UNIVERSITÀ DEGLI STUDI DI PADOVA

Dipartimento di Fisica e Astronomia "Galileo Galilei"

Master Degree in Physics

Final Dissertation

EVOLUTION AND FINAL FATES OF MASSIVE STARS

Thesis supervisor	Candidate
Prof. Paola Marigo	Guglielmo Volpato

Academic Year 2019/2020

To my parents

SYNOPSIS

Stars are the fundamental dowels of the Universe. Their evolution primarily depends on their zero-age-main-sequence mass M_{ZAMS}, i.e. when they start to burn hydrogen in their central cores. Stars are usually classified in three groups. Low-mass stars have $0.8\,M_{\odot} < M_{ZAMS} \lesssim 2\,M_{\odot}$, intermediate-mass stars cover a mass range $2\,M_{\odot} < M_{ZAMS} \lesssim 8\,M_{\odot}$, and massive stars include stars with $8\,M_{\odot} \lesssim M_{ZAMS} \lesssim 100\,M_{\odot}$. Massive stars evolve through all the stable nuclear burning stages, namely H-, He-, C-, Ne-, O- and Si-burning, and their evolution goes on until an iron core is formed, which then becomes unstable and eventually leads to the explosion of the star as a core-collapse supernova.

The study of massive stars is relevant to very different astrophysical aspects: from the production of neutron stars and black holes, which are sources of gravitational-waves (Abbott et al. 2016a; 2016b; 2017; Abbott et al. 2020), to the synthesis of most of the elements in the Universe; they are thought to be the progenitors of long gamma-ray burst events and through their strong stellar winds and supernova explosions they induce star formation and mixing of the interstellar matter.

In my Master thesis I modelled the evolution of massive stars from the pre-main sequence to the end of the Si-burning stage. To this aim I used the stellar evolution code MESA to compute a total of 27 models organized in 4 sets according to the initial metallicity Z (the mass fraction of all species other than H and He) and the helium abundance Y. Each metallicity set ($Z = 0.001, 0.006, 0.014, 0.02$) consists of 6 stellar models with initial mass of 15, 18, 25, 30, 40 and $60\,M_{\odot}$. For $Z = 0.001$ three additional choices of physical parameters are included. Specifically, we considered two rotating models, with initial mass $30\,M_{\odot}$ and $60\,M_{\odot}$ respectively, and also the case of a $60\,M_{\odot}$ star with a modified version of the rate for the nuclear reaction $^{12}\mathrm{C}(\alpha,\gamma)^{16}\mathrm{O}$. The test rate for the aforementioned reaction is smaller by $\sim 42.44\%$ compared with the default rate at temperature $T = 10^9\,K$.

One crucial factor that affects the evolution of massive stars is mass loss caused by stellar winds. Two types of winds are commonly distinguished, which take place when a massive star appears as either a blue supergiant or a red supergiant, when the effective temperature is higher or lower than $\sim 10^4\,K$ respectively. Both kinds of stellar wind can produce mass loss rate up to $10^{-5}\,M_{\odot}/yr$.

In hot luminous stars the wind is driven by line radiation pressure. Photons and ions can interact by absorption and scattering in the stellar atmosphere producing a p-cygni profile with a red-shifted emission. In this way momentum is transferred from the photons to the ions and then is distributed to the whole atmospheric gas through Coulomb interaction. The Doppler effect plays a fundamental role in making these lines efficient in driving the wind. Since the photosphere of the star is receding with respect to atoms in the atmosphere, photons with higher and higher energy are absorbed by ions in order to make a specific transition as long as we consider layers with greater and greater distance from the star. This makes it possible for the atoms to always absorb non-attenuated energy from the photosphere and so the radiation force onto these ions is such that a line driven wind efficient enough can set in and make the star lose mass.

In respect to red supergiant stars, stellar winds are due to absorption of photons by dust grains, which can form in the outer layers of the atmosphere since the temperature is low enough. Differently from the line driven wind, here the Doppler effect is not important. Because of the very low velocity that the wind can reach, the Doppler shift is so small that it does not change significantly the frequency of the absorbed photons.

As the grains are accelerated outwards by photons absorption, they start to interact with gas molecules in the atmosphere. Whether or not this interaction is sufficient to drive the wind critically depends on the density of the wind. Stellar pulsations can lift enough matter to make the dust-molecules coupling high enough to drive the wind. For this reason dust driven winds are referred to as pulsation assisted dust driven wind.

Two special classes of massive stars are Wolf-Rayet and luminous blue variable. The first ones are hot luminous stars that experienced such a high mass loss during their evolution that the external layers are ripped off and the internal ones are exposed to the surface. There are 4 major types of WR stars: WNL, WNE, WC and WO. These are thought of as an evolutionary sequence of deeper and deeper layers being exposed: the WNL and WNE correspond to layers influenced by H burning while the latter types show layers with enhanced abundances of elements produced by He burning. Regarding luminous blue variable stars, this kind of objects are unstable massive stars that undergo episodic mass loss with rate up to $\dot{M} \gtrsim 10^{-3}\, M_{\odot}/yr$. Their instability is due to the luminosity being very close to the Eddington limit. These stars never become red supergiant and reach the WR phase very soon during their evolution.

The central evolution of a massive star is characterized by 6 stable core burning phases: H, He, C, Ne, O and Si. The first one, which coincides with the main sequence (MS) phase of the stellar evolution, is powered by the carbon-nitrogen-oxygen (CNO) cycle. The duration of the H core burning depends on the initial mass ($\propto M^{-2.5}$), during which the luminosity of the star increases and its effective temperature decreases. Among my models only the two rotating ones become WR stars during this burning phase due to their higher mass loss rates enhanced by the rotation. These two are the only models that have a luminosity comparable with the Eddington limit during the evolution, and because of that they become WR stars so early in the H core burning phase.

After the central depletion of the hydrogen, the H burning shifts into a shell surrounding the hydrogen exhausted core, which contracts and heats up until the He starts to burn. In such stars the He burning occurs in a stable manner through the so called triple-α reaction. Also during this phase the mass loss is efficient either due to line driven wind or dust driven wind. Two other models become WR stars during He core burning: the $60\, M_{\odot}$ models with $Z = 0.02$ and with $Z = 0.014$. Similarly to H burning, when the He is exhausted in the core, this latter being mainly composed of carbon and oxygen, the He burning shifts to shell around it.

All the other stable burning phases are called advanced nuclear burning stages. During them the neutrino emission from pair production become important, so that the rate of energy loss in the form of neutrinos exceeds by order of magnitude the luminosity radiated from the surface and hence the evolution of the star is accelerated enormously. The first one of these advanced stages is the C burning. It occurs in a radiative or a convective environment depending on whether the initial mass of the star is below or above the threshold mass $M \sim 20\, M_{\odot}$. The core at C depletion has a composition of mostly oxygen and neon.

After the C burning the next element that starts to burn is the neon followed immediately after by the oxygen. Neon, together with Si, does not burn through direct nuclear fusion but through a complex series of photodisintegration and α-capture. As before, for both Ne and O the central burning then shifts outwards and thus the shell burning phase begins. After the O burning phase the core is composed roughly at 90% by silicon and sulfur.

The last nuclear element that burns in the core is Si. As the Ne, this burning phase occurs through photodisintegration and α-capture, due to the prohibitively high Coulomb barrier for the direct fusion of Si into Ni. When also this burning is over, the presupernova configuration of the star is described by the so called onion-skin structure, which is characterized by concentric burning shells with a central degenerate iron core.

Once reached the pre-supernova stage the iron core becomes unstable due to partial photodisintegration of heavy nuclei and electron captures which progressively reduce the electron degenerate pressure available to sustain the star. So the iron core collapses until a quasi-nuclear density of the matter is reached. The incompressibility of this matter halts the collapse of the inner core, which bounces back creating a shock front. The shock starts to propagate into the still infalling layers of the outer core until it becomes a stalled accretion shock due to energy loss into photodisintegration of iron nuclei into nucleons. Afterwards, a great amount of neutrinos streams away from the just formed proto-neutron star. The so called neutrino heating phase has begun and the stalled shock starts to receive energy from the neutrinos. If the heating is strong enough, the post-shock pressure can overcome the pressure from infalling material and push outwards the shock launching the explosion of the star.

Distinguishing between progenitors that explode as a supernova and those that produce a stellar black hole is one of the most difficult task in stellar astrophysics. From recent hydrodynamical models of explosion O'Connor & Ott (2011) and Ertl et al. (2016) propose, respectively, a single-parameter and a two-parameter classification to test the explodability of massive stars.

O'Connor and Ott define the compactness parameter as:

$$\xi_M \;=\; \left.\frac{M/M_\odot}{R(M_{bary}=M)/1000\,km}\right|_{t=t_{bounce}},$$

with fiducial mass $M \;=\; 2.5\,M_\odot$. This compactness correlates with the density gradient outside the iron core: it is small when the density falls off rapidly with the radius and greater when the gradient is shallow (Sukhbold and Woosley 2014). They have noticed that their models can be subdivided into two different groups: those with $\xi_{2.5} \lesssim 0.45$ and those with $\xi_{2.5} \gtrsim 0.45$. The former group includes less compact models that are expected to produce successful supernovae, the latter contains more compact models that are likely to avoid the explosion and collapse to black holes. Such classification therefore suggests a threshold at $\xi_{2.5} \sim 0.45$ that separates exploding and non-exploding models.

Ertl et al. (2016) introduce two parameters, M_4 and μ_4, evaluated at the presupernova stage. The first one is the enclosed mass for a dimensionless entropy per nucleon $s \;=\; 4$:

$$M_4 \;=\; m(s=4)/M_\odot;$$

while the second is the normalized mass derivative at this location:

$$\mu_4 \;=\; \left.\frac{dm/M_\odot}{dr/1000\,km}\right|_{s=4}.$$

In the framework of neutrino-driven supernova models, the threshold for a successful explosion is the critical neutrino luminosity $L_{\nu,crit} \;\propto\; M_{NS}\dot{M}$, where M_{NS} is the neutron star mass that acts as an

accretor during the neutrino heating phase and $\dot{M}$ is the mass accretion rate. Whenever the progenitor reaches this threshold, the shock is revived and the explosion is launched. Here $L_{\nu,crit}$ can be rewritten as a function of the two parameters defined above: $L_{\nu,crit} \propto M_4\mu_4$, since M_4 is a good proxy for the neutron star mass and μ_4 represents its accretion rate.

There is a correspondence between the $L_\nu - \dot{M}$ and the $M_4\mu_4 - \mu_4$ plane; where the critical threshold $L_{\nu,crit}$ is mapped into a curve of the form: $y_{sep}(x) = k_1 x + k_2$, with $x = M_4\mu_4$, $y = \mu_4$, and k_1 and k_2 are two fitting coefficients (see Sect. 2.3 for further details). This curve therefore separates the progenitors of a successful SN explosion from those that produce a BH. It follows that the $M_4\mu_4 - \mu_4$ plane is a useful diagnostic to assess the final fate of the models.

The main results can be summarized as follows.

- According to the $\xi_{2.5}$ classification out of 27 models 9 will explode as a SN: all the $15\,M_\odot$ stars, all the $18\,M_\odot$ models except the one with metallicity $Z = 0.001$, the $25\,M_\odot$ model with $Z = 0.006$ and the $60\,M_\odot$ star with $Z = 0.014$.

- All three extra models in the lower metallicity set do form a BH: the compactness parameter increases approximately by $\sim$ 96% for the $30\,M_\odot$ model with rotation. In the case of the $60\,M_\odot$ star both rotation and the test rate decrease the compactness parameter: by $\sim$ 10.7% and $\sim$ 66.15% respectively. However, such decrease of $\xi_{2.5}$ is not sufficient to lead to a successful explosion.

- Considering the $M_4 - \mu_4$ classification, only 3 models do produce a SN explosion according to all five possible separation lines: $15\,M_\odot$ star with $Z = 0.006$, $15\,M_\odot$ star with $Z = 0.02$ and $18\,M_\odot$ star with $Z = 0.014$. For two separation lines the $18\,M_\odot$ $Z = 0.02$ model explodes while the $60\,M_\odot$ one with $Z = 0.001$ does it for three possible separation lines.

- In the case of the $30\,M_\odot$ model the rotation does not change the outcome, although there is an increment of $\sim$ 380% in $x = M_4\mu_4$ and $\sim$ 365% in $y = \mu_4$; for the $60\,M_\odot$ model both the rotation and the different rate modify the progenitor's structure such that it shifts into the BH forming region in the $M_4\mu_4 - \mu_4$ plane; with rotation there is an increment of $\sim$ 33% in x and $\sim$ 34% in y, while in the different rate case the increment is about of $\sim$ 50% and $\sim$ 100% respectively.

- Out of 27 models there are 6 models that have a different fate depending on which criterion is considered.

- SN models in my grid are expected to produce NS with masses in the range from $\sim 1.5\,M_\odot$ to $\sim 1.7\,M_\odot$. Such values overlap with the estimated interval of NS masses ($\sim 1.1 - 1.6\,M_\odot$) derived from the NS-NS merger event (GW170817, Abbott et al. 2017)

- BH with masses of $\sim 36\,M_\odot$ and $\sim 29\,M_\odot$, that characterize the components of the BH-BH merger (GW150914, Abbott et al. 2016) are expected to be produced by my models with $M_{ZAMS} = 30, 40\,M_\odot$ and $Z = 0.001$, $M_{ZAMS} = 30, 40\,M_\odot$ and $Z = 0.006$, $M_{ZAMS} = 40, 60\,M_\odot$ and $Z = 0.014$.

- Just recently, another merging event between two compact objects has been detected (GW190814, Abbott et al. 2020). The BH component with mass of $\sim 23\,M_\odot$ is consistent with a stellar progenitor of $M_{ZAMS} = 25\,M_\odot$ and $Z = 0.001$, $M_{ZAMS} = 25\,M_\odot$ and $Z = 0.006$,

$M_{ZAMS} = 30\,M_{\odot}$ and $Z = 0.014$, $M_{ZAMS} = 40, 60\,M_{\odot}$ and $Z = 0.02$. As to the other mysterious compact object of mass $\sim 2.6\,M_{\odot}$, I notice that an iron core of similar mass is left at the end of the pre-supernova evolution of the model with $M_{ZAMS} = 60\,M_{\odot}$ and $Z = 0.02$.

The two-parameter classification should provide a better explodability criterion since accounts for both effects of having a high mass accretion rate. On one hand the neutrino luminosity is enhanced and so during the heating phase a greater amount of energy is available to reenergized the stalled shock and launch the explosion of the star; on the other hand the outgoing shock has to overcome a higher ram pressure due to the infalling layers before reaching the stellar surface.

High compactness $\xi_{2.5}$ shows a tendency to correlate with BH formation, but in the $M_{ZAMS} - \xi_{2.5}$ plane there is not a sharp boundary value that separates explosions from non-explosions (Ugliano et al. 2012; Ertl et al. 2016). In the $M_4\mu_4 - \mu_4$ plane this separation does exist and it is represented by the separation line.

In this work I do not use a dynamical code to simulate the collapse and explosion of my models, and so there is no way to have a robust check of the predicted outcomes. This would be the next step to further investigate the explodability of the progenitors presented here. Both classifications are developed from a 1D modeling approach that can not take into account multi-dimensional effects and moreover the neutrino mechanism at the base of the SN explosion is not fully understood yet. However, substantial progress has been made in higher dimensions simulations which are expected to improve the understanding of the physical processes involved in both SN explosions and BHs formation. Hopefully in the future large sets of 3D explosion simulations will be feasible eventually leading to the much needed advancement in stellar explodability classification.

Contents

Chapter 1

The Evolution of Massive Stars

The primary parameter that controls the evolution of stars is the initial mass at the zero age main sequence (ZAMS), when starts to burn hydrogen in their central core. Stars with $0.8\,M_{\odot} < M_{ZAMS} \lesssim 2\,M_{\odot}$ are classified as low-mass stars, these develop a degenerate helium core once the main sequence phase is over and hence the helium ignition is unstable and occurs through a thermal instability, the helium flash, at the tip of the Red Giant Branch. For M_{ZAMS} between $\sim 2\,M_{\odot}$ and $\sim 8\,M_{\odot}$ the helium is ignited in a stable manner since the helium core avoids electron degeneracy after the main sequence. These intermediate-mass stars form a carbon-oxygen core which becomes degenerate and end their lives through the same evolutionary channel as low-mass stars. The stellar envelope is removed by stellar winds while the bare core becomes a C-O white dwarf. Massive stars are defined as those stars with $M_{ZAMS} \gtrsim 8\,M\odot$, that ignite carbon in a non degenerate core. With the only exception of stars with $8\,M_{\odot} < M_{ZAMS} \lesssim 11\,M_{\odot}$, massive stars evolve through all the stable nuclear burning stages and never experience a significant electron degeneracy in their core during them. The upper limit for the mass of massive stars is usually $\sim 100\,M_{\odot}$, while stars with $100\,M_{\odot} < M_{ZAMS} \lesssim 10^4\,M_{\odot}$ are called very massive stars. The evolution of massive stars goes on until an iron core is formed, which then becomes unstable and eventually leads to the explosion of the star as a core-collapse supernova (CCSN).

These objects are of paramount importance for the evolution of the Universe for several reasons: through strong stellar wind and supernova explosion they induce star formation and mixing of the interstellar matter (Girichidis et al. 2020), they produce neutron stars (NS) and black holes (BH) and synthesize most of the elements present in the Universe, including those necessary to life, throughout their evolution and final explosion (Woosley et al. 2002). Moreover, they are responsible for the reionization of the Universe at redshift $z > 5$ and the pregalactic chemical enrichment (Topping et al. 2020); they might be involved in the production of massive black holes ($M \gtrsim 10^6\,M_{\odot}$) that are thought to be the progenitors of active galactic nuclei (Valiante et al. 2017; 2018a; 2018b); finally massive stars produce long-lived radioactive isotopes, e.g. ^{26}Al, ^{56}Co, ^{60}Fe , and are the progenitors of gamma-ray burst (Nomoto 2012).

In the following sections I will present and discuss the pre-supernova evolution. Particular attention will be devoted to describe mass loss by stellar winds, and the sequence of hydrostatic nuclear burnings up to the formation of the iron core.

1.1 Evolutionary Calculations

In my Master thesis I modelled the evolution of massive stars. To this aim I adopted the stellar evolution code MESA (see Chapt. 3 for a brief introduction to this stellar evolution code and the adopted physics used to compute the models and see also Paxton et al. 2011; 2013; 2017; 2018; 2019 for detailed description of various MESA implementations). I computed 27 stellar models, which are arranged in 4 sets according to the initial metallicity Z (the mass fraction of all species other than H and He) and the helium fraction Y. Each set is composed of 6 models with mass 15, 18, 25, 30, 40 and $60\,M_{\odot}$ plus three special models in the lower metallicity set (see Table 1.1 below).

Table 1.1: Summary of all the 27 models calculated for this work. The special ones include rotating models ($M_{ZAMS} = 30$ and $60\,M_{\odot}$ with $Z = 0.001$) and the case of a test rate for the reaction $^{12}\mathrm{C}(\alpha,\gamma)^{16}\mathrm{O}$ applied to the model with $MZAMS = 60\,M_{\odot}$ and $Z = 0.001$ (see Sect. 3.1.3). They are called 30.rot, 60.rot and 60.cf88 respectively.

initial composition	initial mass $[M_{\odot}]$	special models
Z=0.001 Y=0.250	15, 18, 25, 30, 40, 60	30.rot, 60.rot, 60.cf88
Z=0.006 Y=0.259	15, 18, 25, 30, 40, 60	
Z=0.014 Y=0.273	15, 18, 25, 30, 40, 60	
Z=0.020 Y=0.284	15, 18, 25, 30, 40, 60	

The mass of each core, e.g. He core mass, CO core mass, Fe core mass, is calculated at the depletion of the burning fuel, e.g H, He and Si respectively, unless stated otherwise. For the computation of the M_4 and μ_4 parameters (Sect. 2.3) I approximate $R_{\odot}$ with the value of $700\,000\,km$.

1.2 Mass Loss

Mass loss during different phases of the evolution of a star is one of the most uncertain ingredient in stellar astrophysics. Especially for massive stars this affects heavily the path of the star across the various core and shell burnings until the formation of the degenerate iron core. Massive stars may experience two types of stellar winds depending on whether the star loses mass as a blue supergiant BSG or a red supergiant RSG. Winds of luminous hot stars are driven by line radiation pressure (Lucy & Solomon 1967). The radiation driven theory was developed by Castor et al. (1975) and then improved through the course of the decades (Abbott 1982; Friend & Abbott 1986; Pauldrach et al. 1986; Kudritzki et al. 1989).

Since stellar photons can be absorbed and scattered by ions, with resonant scattering being the main mechanism in the formation of spectral lines, there is a momentum transfer to the gas particles which then share it through Coulomb interaction with the whole plasma. The radiation force onto these ions, however, would not be so efficient if the Doppler effect were not present. This latter makes it possible for atoms to absorb non-attenuated continuum photons, due to Thomson scattering, at every layer of the stellar atmosphere. Due to the fact that for atoms in the outer atmospheric layers the photosphere is receding, photons with higher and higher energy will be absorbed in order to a specific transition line to occur as one moves outwards in the stellar atmosphere; thus strong spectral lines are very efficient in driving the wind of these hot and luminous massive stars. The lines that

contribute the most are those of the metals and also of C, N and O; while H and He contribute very little and only for stars with $T_{eff} \lesssim 6000\,K$ due to their highly ionized state (Lamers 2007).

Regarding luminous cool giant stars, RSG, radiative driving that triggers the wind is due to absorption of photons by dust grains in the outer layers of the stellar atmosphere (Lamers & Cassinelli 1997). One major difference with respect to the line driven wind of hotter stars, is that the Doppler shift does not play a crucial role but rather it is quite unimportant. This difference is caused by the fact that the terminal velocity reaches very high values in line driven winds, $\gtrsim 10^3\,km/s$, but it is much lower in cooler stars that develop dust driven winds, $\lesssim 30\,km/s$. However, both kinds of wind can generate very high mass loss rate up to $10^{-5}\,M_{\odot/yr}$.

In such cool stars the low effective temperature allows the formation of dust grains, which absorb momentum from the radiation field of the photosphere and are accelerated outwards. There are two main kinds of grains: silicate grains and carbonaceous grains. Whether the first or the second one is formed depends on the carbon-oxygen ratio at the star photosphere. As more and more grains are accelerated they start to interact with the gas molecules of the stellar atmosphere and if the coupling between dust and gas is sufficient then the wind can be driven properly. This coupling depends on the wind density. In dust driven wind there is another mechanism that plays a fundamental role other than the dust: stellar pulsations. Through pulsations enough matter can be lifted onto the upper layers of the atmosphere and thus there is sufficient coupling between dust grains and gas molecules to drive the wind, similarly to the case of Asymptotic Giant Branch stars (Mauron & Josselin 2011).

1.2.1 Wolf-Rayet and Luminous Blue Variable Stars

Wolf-Rayet (WR) stars are hot luminous stars with bright emission lines in their spectra (first observations by Wolf & Rayet 1867). This kind of stars are characterized by strong line driven winds, in which multiple photon scattering plays a fundamental role, that produce very efficient mass loss reaching rates as high as $\dot{M} \sim 10^{-5} - 10^{-4}\,M_{\odot}/yr$.

Such strong mass loss exposes the H or even the He burning core of a massive stars enhancing therefore the surface abundances of elements produced by either of the two fusion processes. According to surface abundance of H, He, N, C and O WR stars are classified into different subtypes. Massive stars with surface H abundance $X_H < 0.4$ and increased abundances of He and N are WNL stars; WNE are similar to these latter but with complete lack of hydrogen, $X_H = 0$. Another type of WR stars that have no hydrogen are the WC stars: they are characterized also by little or even absent N and increased abundances of He, C and O; finally similar to WC stars but with significantly higher O abundance there are the WO stars.

These WR subtypes are thought of as an evolutionary sequence of deeper and deeper layers of the star being exposed as consequence of mass loss. Meaning that the first types correspond to the exposure of layers modified by the H burning, while latter types show stellar layers corresponding to the He burning.

In Fig. 1.2 there are the HR diagrams of all the models that become WR stars during their evolution. The different WR phases are labeled with the corresponding subtype name according to abundance-based classification in Georgy et al. (2015) and Meynet & Maeder (2003). The H abundance upper limit is not quite established since it can be either $X_H < 0.4$ or $X_H < 0.3$. I

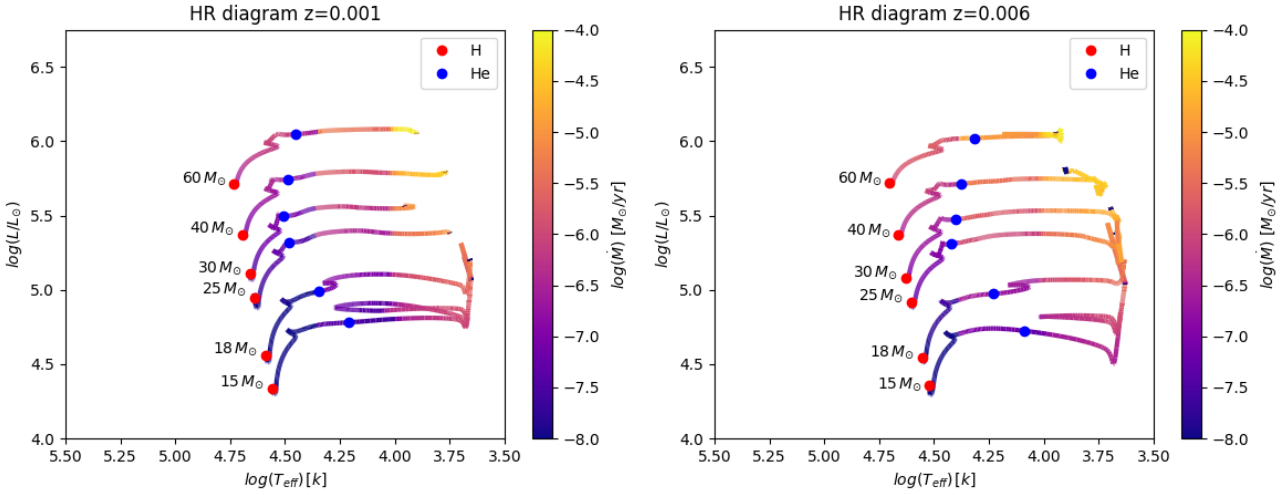

(a)

(b)

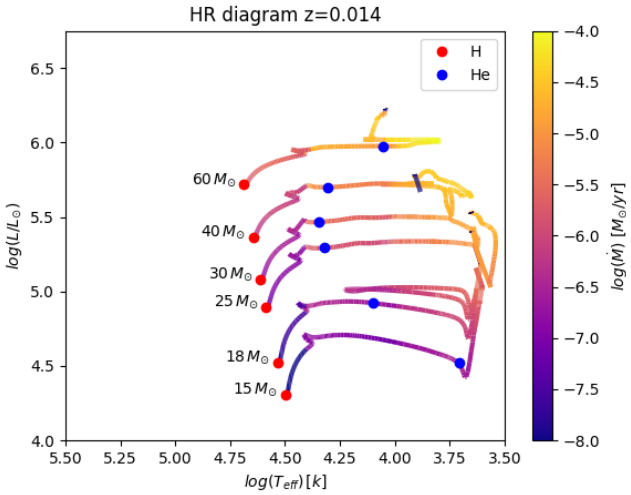

(c)

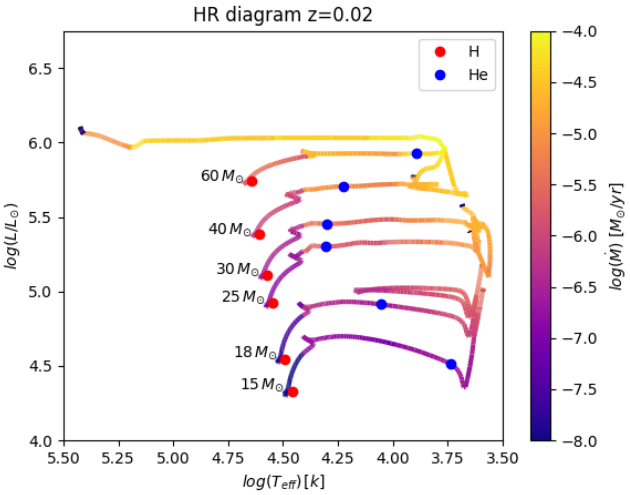

(d)

Figure 1.1: Evolutionary tracks of massive stars in the HR diagram, from the main sequence up to the end of the Si-burning phase. The tracks are color-coded according to mass-loss rate. The onset of H and He-burning is marked with a red and a blue dot, respectively. The initial masses are indicated nearby the corresponding track. The four panels show the results for four choices of the initial metallicity, namely $Z = 0.001$, $Z = 0.006$, $Z = 0.014$ and $Z = 0.02$.

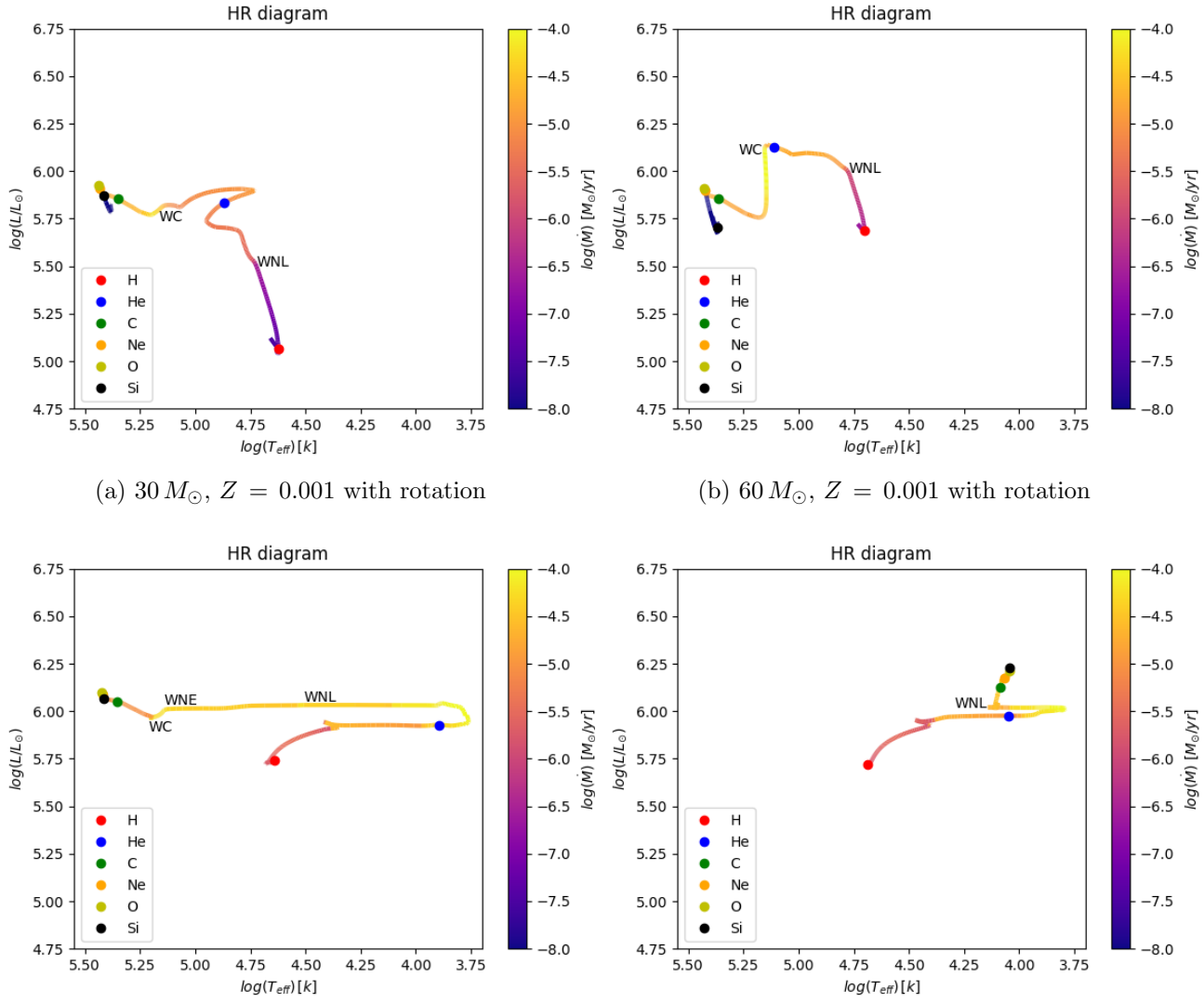

(a) $30\,M_{\odot}$, $Z = 0.001$ with rotation

(b) $60\,M_{\odot}$, $Z = 0.001$ with rotation

(c) $60\,M_{\odot}$, $Z = 0.02$

(d) $60\,M_{\odot}$, $Z = 0.014$

Figure 1.2: Evolutionary tracks in the Hertzsprung-Russell diagram of stellar models indicating the subsequent WR phases during the evolution. Tracks are color-coded as a function of the current mass-loss rate (right color bars).

adopted the first one and because of that the $60\,M_{\odot}$ model with $Z = 0.014$ (Fig. 1.1c) can be classified as a WNL star by the end of its He burning phase.

Another class of stars characterized by huge mass loss are the luminous blue variables (LBVs). These unstable massive stars undergo episodic mass loss with $\dot{M} \gtrsim 10^{-3}\,M_{\odot}/yr$. The instability is due to fact that, during some phases of their evolution, such stars have a luminosity close to the Eddington limit:

$$L_{Edd} = \frac{4\pi cGM}{k_e}, \tag{1.1}$$

where k_e is the electron-scattering opacity, c is the speed of light in vacuum, G is the universal gravitational constant and M is the current mass of the star, and this may lead to a violation of the hydrostatic condition in the external layers. Stars that experience LBV mass loss outbursts become WR stars without ever reaching the red supergiant phase.

Among the presented models only the two rotating stars with mass $30\,M_{\odot}$ and $60\,M_{\odot}$ (Fig. 1.2a and 1.2b respectively) reach luminosities of order $\sim 0.8\,L_{Edd}$. The former during H and He burning phase goes from $\sim\ 0.3\,L_{Edd}$ to $\sim\ 0.8\,L_{Edd}$, while the latter, during the main sequence and the He burning, goes from $\sim\ 0.5\,L_{Edd}$ to $\sim\ 0.8\,L_{Edd}$; none of them experiences mass loss rates higher than $\sim\ 10^{-4}\,M_{\odot}/yr$.

1.2.2 Mass Loss prescriptions

Stellar evolution models are computed adopting a combination of radiative wind prescriptions, collectively called the *Dutch* mass loss scheme in MESA (based on Glebbeek et al. 2009). I adopt the overall scaling factor $\eta_{Dutch}\ =\ 0.8$ (like for the two models discussed in section 6.1 of Paxton et al. 2017).

This *Dutch* scheme consists of three different regimes:

1. For $T_{eff}\ >\ 1.1\cdot 10^4\,K$ and X_{surf} (surface hydrogen mass fraction) $>\ 0.4$, mass loss prescription from Vink et al. (2000; 2001) is employed.

   For $2.75\cdot 10^4\ <\ T_{eff}\ <\ 5\cdot 10^4\,K$,

$$\begin{aligned}\dot{M}_{V,hot}\ =\ & 10^{-6.697}\cdot(L/10^5\,L_{\odot})^{2.194}\cdot(M/30\,M_{\odot})^{-1.313}\cdot\Big(\frac{v_{\infty}/v_{esc}}{2.0}\Big)^{-1.226}\cdot\\ & \cdot(T_{eff}/4\cdot 10^4\,K)^{0.933}\cdot 10^{-10.92[log(T_{eff}/4\cdot 10^4\,K)]^2}\cdot(Z_{surf}/Z_{\odot})^{0.85}.\end{aligned}\tag{1.2}$$

   The ratio of terminal velocity to the escape velocity increases with metallicity as $v_{\infty}/v_{esc}\ =\ 2.6(Z_{surf}/Z_{\odot})^{0.13}$.

   For $1.1\cdot 10^4\ <\ T_{eff}\ <\ 2.25\cdot 10^4\,K$, [1]

$$\begin{aligned}\dot{M}_{V,cool}\ =\ & 10^{-6.688}\cdot(L/10^5\,L_{\odot})^{2.210}\cdot(M/30\,M_{\odot})^{-1.339}\cdot\Big(\frac{v_{\infty}/v_{esc}}{2.0}\Big)^{-1.601}\cdot\\ & \cdot(T_{eff}/4\cdot 10^4\,K)^{1.07}\cdot(Z_{surf}/Z_{\odot})^{0.85},\end{aligned}\tag{1.3}$$

   where $v_{\infty}/v_{esc}\ =\ 1.3(Z_{surf}/Z_{\odot})^{0.13}$.

   For $2.25\cdot 10^4\ <\ T_{eff}\ <\ 2.75\cdot 10^4\,K$, either $\dot{M}_{V,hot}$ or $\dot{M}_{V,cool}$ is adopted depending on the exact position of the so-called bi-stability jump, a phenomenon in which $\dot{M}$ increases with decreasing T_{eff} due to the recombination of metal lines:

$$T_{eff,jump}\ =\ 61.2+2.59\,log\langle\rho\rangle,\tag{1.4}$$

   where $\langle\rho\rangle$ corresponds to the characteristic wind density at 50% of the thermal velocity of the wind.

[1] In Vink et al. (2001), mass loss rates were computed for $T_{eff}\ \geq\ 1.25\cdot 10^4\,K$, but the prescription is extended down to $T_{eff}\ =\ 1.1\cdot 10^4\,K$ in MESA.

2. Within the previous temperature range ($T_{eff} > 10^4\,K$) but with $X_{surf} < 0.4$, the star is formally identified as a WR star and hence it is adopted the empirical mass loss prescription from Nugis & Lamers (2000):

$$\dot{M}_{NL} = 10^{-11}(L/L_\odot)^{1.29} X_{surf}^{1.7} Z_{surf}^{0.5}\, M_\odot/yr. \tag{1.5}$$

3. For all stars with[2] $T_{eff} < 10^4\,K$, including stars in the RSG phase, I use the de Jager et al. (1988) empirically derived wind prescription:

$$\dot{M}_{dJ} = 10^{-8.158}(L/L_\odot)^{1.769} T_{eff}^{1.676}\, M_\odot/yr. \tag{1.6}$$

Our present understanding is that stellar winds from RSGs is driven by dust. The low temperatures and pulsations in the outer layers lead to condensation of dust at large radii, which is then driven out due to radiation pressure on grains (Mauron & Josselin 2011).

1.2.3 Rotationally enhanced Mass Loss

Mass loss enhanced by rotation is a key ingredient for rotating models since it can change significantly the evolution of the star (Heger et al. 2000). In MESA this enhancement is implemented through a function of the surface angular velocity Ω:

$$\dot{M}(\Omega) = \dot{M}(0)\big(\frac{1}{1-\Omega/\Omega_c}\big)^{\xi}, \tag{1.7}$$

where $\dot{M}(0)$ is the *Dutch* mass loss rate, ξ is equal to 0.43 (Friend & Abbott 1986) and Ω and Ω_c are respectively the surface angular velocity and the surface critical angular velocity (Eq. 3.3). The maximum rotational boost allowed is 10^4, in order to avoid too high mass loss rates.

1.3 H burning

Core hydrogen (H) burning is the first stable nuclear burning stage and it corresponds to the main sequence (MS) phase of the star. In massive stars it is powered by the carbon-nitrogen-oxygen (CNO) cycle given the high central temperatures attained in the core. The CNO cycle main reactions are:

[2]In MESA, mass loss rate for $10^4 < T_{eff} < 1.1 \cdot 10^4$ is computed by smoothly transitioning between the low temperature prescription (3.) and the high temperature prescription (1. or 2.).

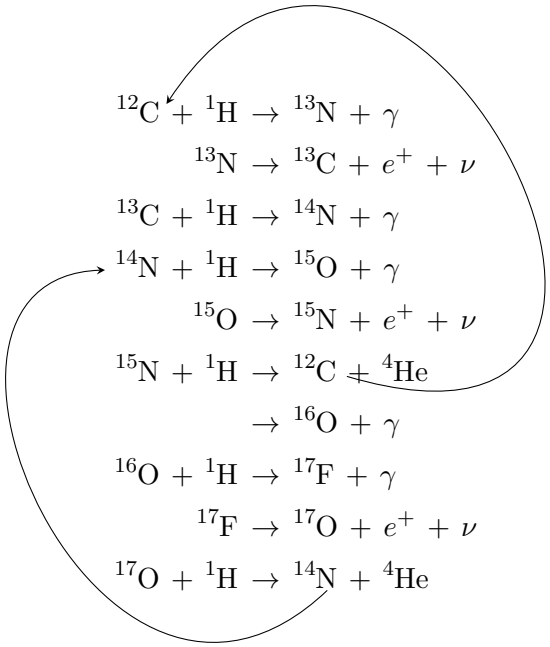

$$
\begin{aligned}
^{12}\mathrm{C} + {}^{1}\mathrm{H} &\rightarrow {}^{13}\mathrm{N} + \gamma \\
{}^{13}\mathrm{N} &\rightarrow {}^{13}\mathrm{C} + e^{+} + \nu \\
{}^{13}\mathrm{C} + {}^{1}\mathrm{H} &\rightarrow {}^{14}\mathrm{N} + \gamma \\
{}^{14}\mathrm{N} + {}^{1}\mathrm{H} &\rightarrow {}^{15}\mathrm{O} + \gamma \\
{}^{15}\mathrm{O} &\rightarrow {}^{15}\mathrm{N} + e^{+} + \nu \\
{}^{15}\mathrm{N} + {}^{1}\mathrm{H} &\rightarrow {}^{12}\mathrm{C} + {}^{4}\mathrm{He} \\
&\rightarrow {}^{16}\mathrm{O} + \gamma \\
{}^{16}\mathrm{O} + {}^{1}\mathrm{H} &\rightarrow {}^{17}\mathrm{F} + \gamma \\
{}^{17}\mathrm{F} &\rightarrow {}^{17}\mathrm{O} + e^{+} + \nu \\
{}^{17}\mathrm{O} + {}^{1}\mathrm{H} &\rightarrow {}^{14}\mathrm{N} + {}^{4}\mathrm{He}
\end{aligned}
\tag{1.8}
$$

and thus the net hydrogen burning reaction is:

$$
4\,{}^{1}\mathrm{H} \rightarrow {}^{4}\mathrm{He} + 2\,e^{+} + 2\,\nu, \tag{1.9}
$$

where the fusion of four ^{1}H nuclei results in a ^{4}He nucleus and two positrons and two neutrinos.

As the CNO cycle has a high sensitivity on T there is a high nuclear energy flux and thus the hydrogen burns in a convective core unlikely in low mass stars where it burns in a radiative one through the proton-proton chain. When the core reaches the H-depletion the hydrogen burning shifts in a shell outside the core and then the H-shell burning phase begins. The duration of the H core burning depends on the initial mass ($\propto M^{-2.5}$), during which the luminosity of the star increases while its effective temperature decreases (see Fig. 1.3). Mass loss can be already effective during hydrogen burning and scales with the mass of the star (and of course the metallicity); for most massive stars ($\gtrsim 60\,M_{\odot}$) with solar and super-solar metallicity it can reach values high enough to induce a substantial reduction of the total mass and thus to expose to the surface the zones modified by the H core burning and so the star becomes a Wolf-Rayet (WR).

In the present set there are two models that become WR stars during this evolutionary phase. The $30\,M_{\odot}$ star and the $60\,M_{\odot}$ star, both with initial metallicity $Z = 0.001$, that have an initial surface angular velocity of $\Omega/\Omega_c = 0.7$ (see Sect. 3.4); while the $60\,M_{\odot}$ star with $z = 0.02$ and the $60\,M_{\odot}$ star with $z = 0.014$ become WR later on during the He core burning (Fig. 1.2). The main effect of rotation, as can be seen, is to evolve the track towards higher luminosity and effective temperature. This different path in the HR diagram enhances the mass loss rate of the models making them become WR stars at a such early phase.

The He core at H depletion depends on the size of the H convective core: the larger its size the larger the region where hydrogen is converted into helium and the same applies to He core at H exhaustion. In general the maximum size of the H convective core increases with the mass of the star and so it does the He core at H core depletion. This behavior is affected by the efficiency of stellar wind: if mass loss is quite stong it may reduce the size of the H convective core. As a consequence the He core is smaller than it would be in case of reduced or absent mass loss (this usually applies to stars with mass $\gtrsim 60\,M_{\odot}$). As metallicity decreases the star becomes more and more compact and

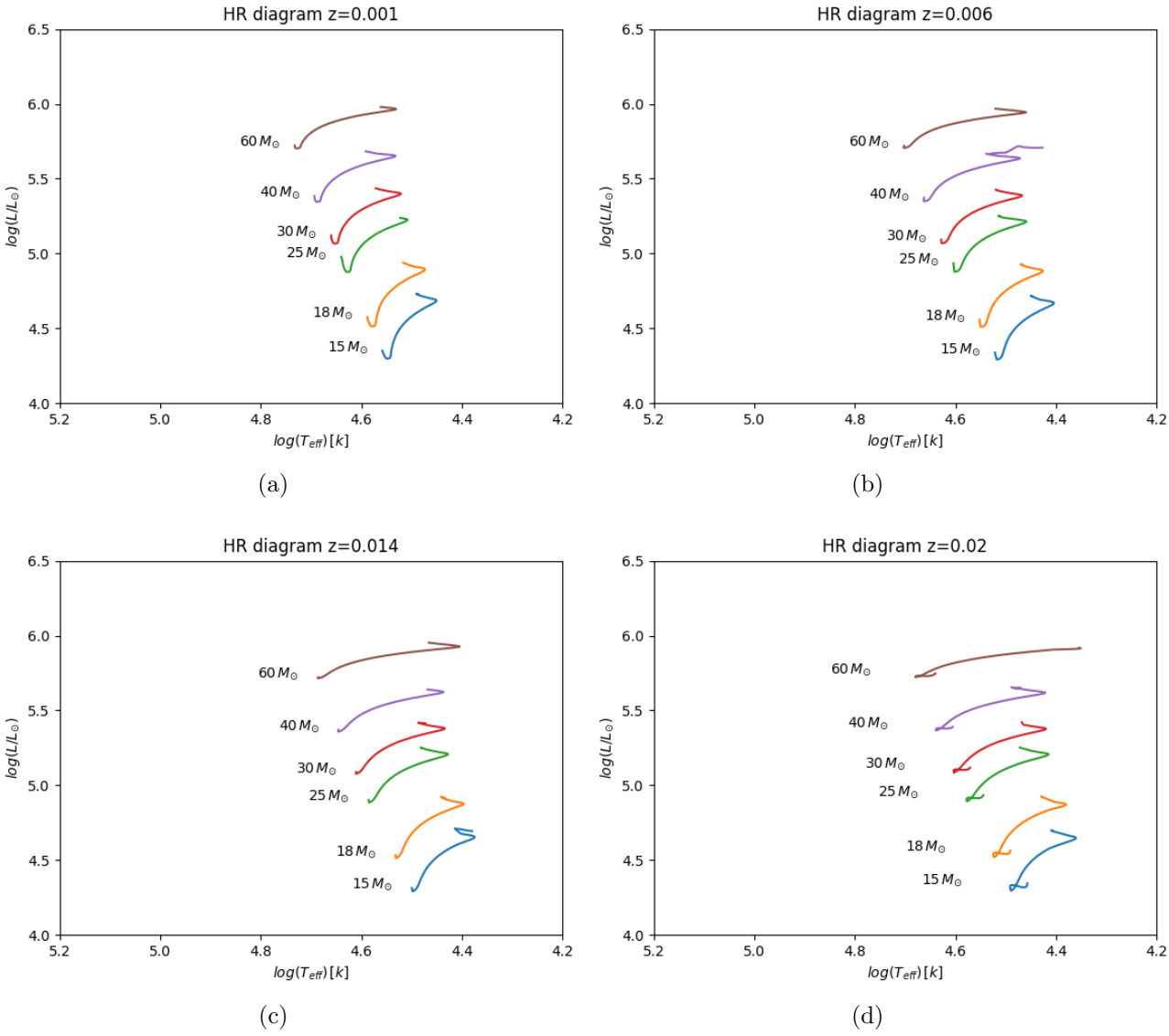

(a) (b)

(c) (d)

Figure 1.3: Hertzsprung-Russel (HR) diagrams of models of indicated metallicities during the hydrogen core burning phase.

hotter due to to reduction of the opacity of the matter; this implies bluer evolution tracks in the HR diagram (Fig. 1.3).

The mass loss scales with metallicity as $\dot{M} \sim Z^{0.85}$, therefore low metallicity stars during H core burning evolve at almost constant mass. This implies also a reduction of the abundance of the CNO nuclei and hence an increase of the core H burning temperature; this means a larger convective H core and so a larger He core at H exhaustion. For stars with $M < 30 - 40\,M_{\odot}$ the He core at H depletion is essentially independent on Z (Fig. 1.4). Conversely, for stars above this limit there are seeable differences depending on metallicity. As can be seen in Fig. 1.4 it is not present the effect described by Limongi (2017) due to mass loss, and the reason for this is because this latter does not reach the core of the star so the M_{He} does not decrease with the increasing of the initial metallicity.

During H core burning rotation-induced mixing provides more fuel to the H convective core and mixes the H burning products into the envelope of the star. The main effects of rotation-induced mixing are the increase of the H burning duration and the increase of the He core mass at H depletion. Due to this latter the He core mass at H depletion increases with the initial rotation velocity. Nevertheless, this effect could be less significant if combined with a high mass loss enhanced by rotation. In this case the H convective core is reduced yielding a smaller He core at H depletion with respect to models without rotation. The combination of these two effects explains the differences between rotating and non rotating models with $30\,M_{\odot}$ and $60\,M_{\odot}$. For the $30\,M_{\odot}$ model there is an increment of $\sim$ 70% in He core mass at H depletion, while for the $60\,M_{\odot}$ model the increment is only about $\sim$ 9% (see Table 1.2). This is due to a higher mass loss rate in the rotating $60\,M_{\odot}$ model with respect to the $30\,M_{\odot}$ one during H core burning as can be seen in Fig. 1.2. Regarding the He core mass at H depletion there are no differences between the 60 and $60.cf88$ models (Table 1.2), since the $^{12}C(\alpha,\gamma)^{16}O$ reaction does not play a role during H core burning.

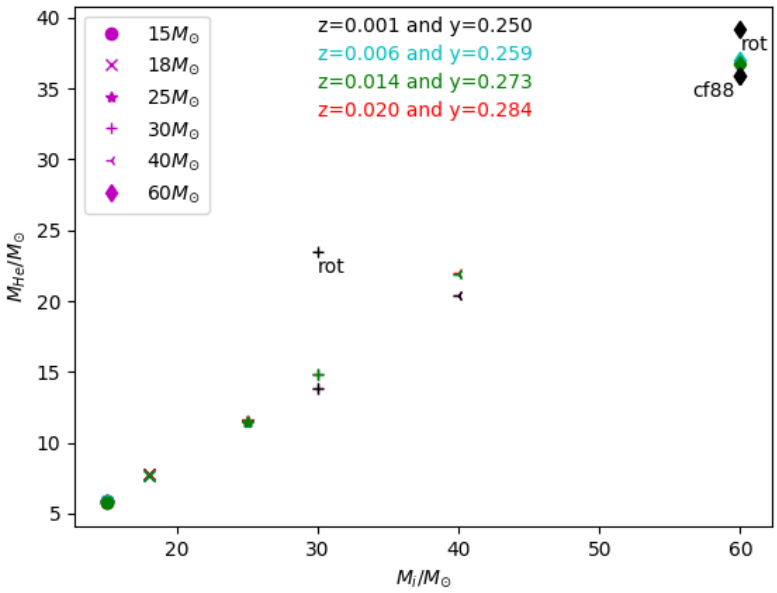

Figure 1.4: He core mass at H core depletion for models with different initial mass and metallicity.

According to the He core mass range for a star to enter the pulsation-pair instability region, $40 \lesssim M_{He} \lesssim 60$, or the pair instability SN, $60 \lesssim M_{He} \lesssim 137$ (Woosley et al. 2007), it is worth

Table 1.2: M_{ZAMS}, He core mass at H depletion, CO core mass at He depletion and Fe core mass at Si depletion for all models in the grid.

	M_{ZAMS} $[M_\odot]$	He core mass $[M_\odot]$	CO core mass $[M_\odot]$	Fe core mass $[M_\odot]$
$Z = 0.001$				
	15	5.899	3.399	1.686
	18	7.744	4.275	1.845
	25	11.492	6.190	1.874
	30	13.836	7.525	2.060
rot	30	23.465	17.860	2.432
	40	20.366	10.284	2.002
	60	35.929	17.496	2.007
rot	60	39.145	17.724	2.100
cf88	60	35.929	17.423	2.197
$Z = 0.006$				
	15	5.856	3.256	1.547
	18	7.652	4.276	1.641
	25	11.441	5.936	1.660
	30	14.835	7.913	1.887
	40	21.891	12.303	2.249
	60	37.001	19.263	2.034
$Z = 0.014$				
	15	5.808	3.159	1.612
	18	7.712	4.165	1.638
	25	11.468	6.467	2.173
	30	14.854	8.114	2.219
	40	21.927	12.264	2.099
	60	36.682	21.415	1.760
$Z = 0.02$				
	15	5.754	3.093	1.568
	18	7.755	4.098	1.646
	25	11.525	6.376	1.830
	30	14.875	8.549	1.906
	40	21.952	12.466	2.201
	60	36.848	24.643	2.634

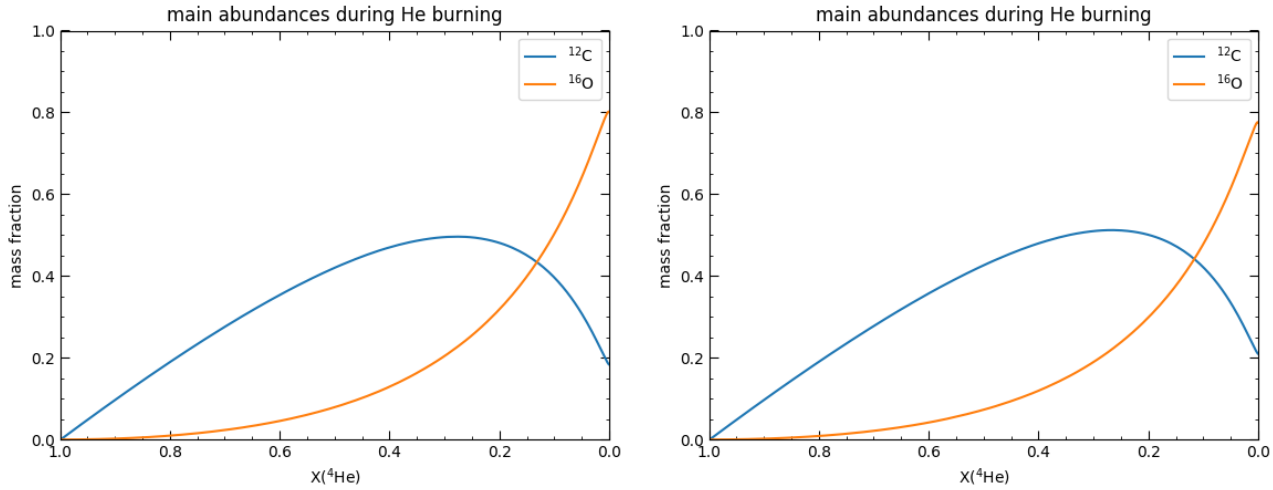

(a) 60 (b) 60.cf88

Figure 1.5: Comparison between models $60\,M_{\odot}$, $Z = 0.001$ (60) and $60\,M_{\odot}$, $Z = 0.001$ with CF88 rate for $^{12}C(\alpha,\gamma)^{16}O$ reaction (60.cf88). In the two figures are plotted abundances of ^{12}C and ^{16}O during He core burning.

noting that none of the 27 models of the present set enters either of them. Only the rotating $60\,M_{\odot}$ model laps the lower limit of the pulsation-pair instability region remaining however in the CCSN regime (see Table 1.2 for the exact M_{He} value at H depletion).

1.4 He burning

After H core depletion, the H burning shell shifts outward in mass and increases the He core mass. During this phase all the non-rotating models move toward lower temperatures in the HR diagram (Fig. 1.6), at constant luminosity, while the He core contracts and heats up until the He burning reactions are activated.

The timescale of this transition phase depends on the efficiency of the chemical mixing in the region left by the receding convective core during H core burning, which is still uncertain and hence its timescale cannot be determined with precision. This zone is a semiconvective region: unstable according to the Schwartzschild criterion, but stable according to the Ledoux one. Adopting the first one, the region is mixed quite efficiently and the redward path in the HR diagram occurs on a nuclear timescale: during the He core burning. Hence the region between the MS and the red giant branch (RGB) would be well populated. Contrariwise, if the second criterion is adopted, the mixing is suppressed and the same evolution toward lower T_{eff} takes place on much faster Kelvin-Helmholtz timescale, so there would be a gap between MS and RGB in the HR diagram. The stabilizing effect of ∇_{μ} may undergo severe reduction and even destruction if there is any kind of turbulence that favors the onset of convection, which in fact reduces even more ∇_{μ}. The only hint that is available nowadays on how to treat the mixing in such a convective region comes from the observations. They show the presence of a gap between MS and RGB in the color-magnitude diagram of massive stars for both the Milky Way and the Magellanic Clouds.

There are two main reactions taking place during He core burning:

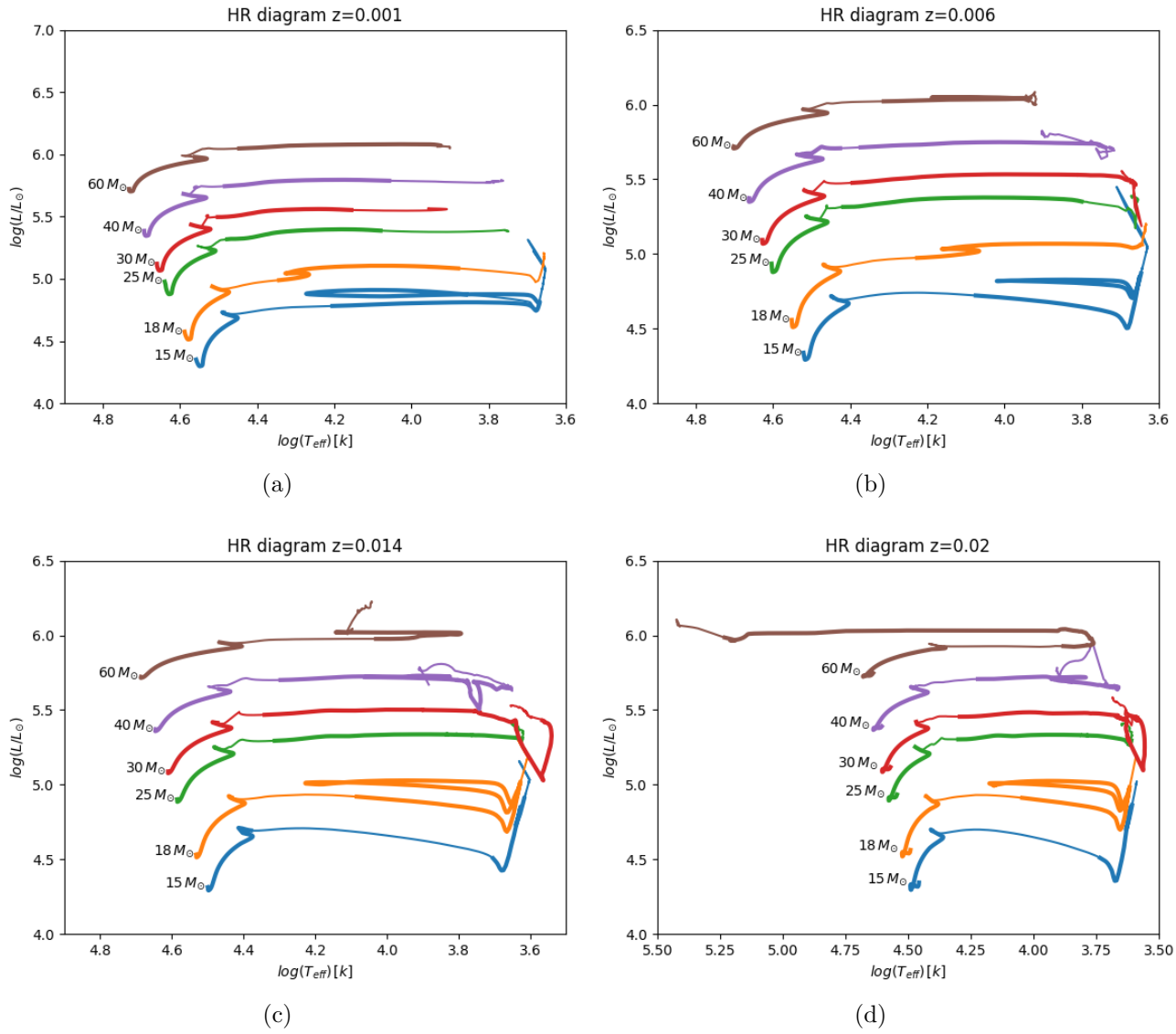

Figure 1.6: Hertzsprung-Russel (HR) diagrams of models of indicated metallicities. The thicker line corresponds to the H core burning and He core burning phases.

$$3\,{}^{4}\mathrm{He} \rightarrow {}^{12}\mathrm{C} + \gamma \tag{1.10}$$

$${}^{12}\mathrm{C} + {}^{4}\mathrm{He} \rightarrow {}^{12}\mathrm{O} + \gamma. \tag{1.11}$$

The first one, called 3α reaction, is the net effect of two α-capture involving ^{4}He and ^{8}Be. Since these two occur almost simultaneously, due to the fact that the ^{8}Be nucleus decays very rapidly, the triple-α reaction can be treated as a single reaction involving three particles. The second reaction (Eq. 1.4) can happen when it is produced enough ^{12}C. The rate of this latter is highly uncertain and affects the competition between the 3α reaction and the production of ^{16}O. In Fig. 1.5 there is the comparison of ^{12}C and ^{16}O abundances during He burning for models with different rates for reaction $^{12}\mathrm{C}(\alpha,\gamma)^{16}\mathrm{O}$. As can be noticed, the differences are very small, but since the CF88 rate is smaller than the default JINA REACLIB rate (see Sect. 3.1.3), the oxygen-to-carbon ratio is lower in the former case.

Referring to Fig. 1.6, the He core burning begins when the star is a BSG or a RSG depending on its initial mass and metallicity. Stars that start He burning as a RSG reach temperatures low enough that allow the formation of dust driven wind, which enables a phase of strong mass loss. The central abundance of He at the onset of the dust driven wind is very important in determining the actual mass lost during the He burning and thus in determining whether the star remains a RSG or becomes a BSG/WR star. If the star begins to lose mass at late stages of the He burning, then throughout the remaining of this burning it will lose a small amount of mass and hence the star will still be a RSG along the subsequent evolution. In the opposite scenario, where the star enters the dust driven wind phase during the early stages of He burning, there is the possibility for the star to lose a considerable amount of its mass. This favors the evolution from a RSG to a BSG/WR star, which is the scenario for the two non-rotating WR models with initial mass of 60 $M_{\odot}$ and metallicity $Z = 0.02$ and $Z = 0.014$.

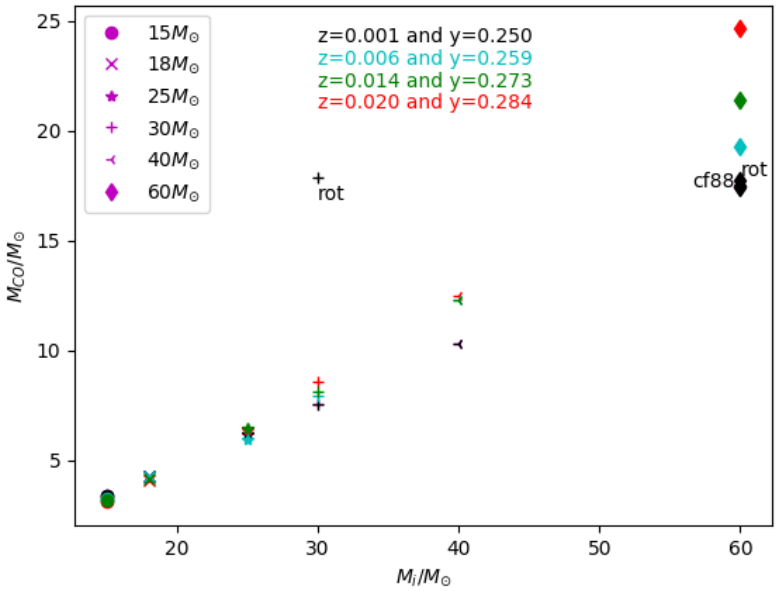

Figure 1.7: CO core mass at He depletion as function of the initial mass and for different metallicity.

Core He burning lasts $\sim 10^6 - 10^5\, yr$ for stars within $15\, M_{\odot} - 60\, M_{\odot}$ and it occurs in a convective core like the previous H core burning. Stars that experience a sufficient mass loss to progressively reduce the He core enter the WNE stage and eventually, if the total mass is reduced below the maximum extension of the He convective core, may become WC stars (Fig. 1.2). As mentioned above, among the non-rotating models only the 60 $M_{\odot}$ star with $z = 0.014$ (Fig.1.6c) becomes a WNL star, while the 60 $M_{\odot}$ star with $z = 0.02$ (Fig. 1.6d) become a WC star. As the He core reduces in mass due to mass loss, the star tends to behave as a lower mass star, i.e. reducing its central temperature. The main effect on the evolution of the star is that the CO core at core He exhaustion is smaller than it would be without mass loss. In my set of models the CO core mass increases with the initial mass and metallicity (Fig.1.7).

The effect of the initial Z on the CO core mass is negligible for star with $M \lesssim 30\, M_{\odot}$. Above this threshold the $M_{CO} - M_{int}$ relation is shallower at super-solar and solar metallicity. This is due to the fact that at low metallicity models evolve at almost constant mass because of their reduced mass loss, on the contrary at higher metallicity the CO core mass is actually reduced. Like mentioned above regarding the He core produced by the H core burning, in Fig. 1.7 there is not the decreasing of the

CO core mass as the metallicity increases because, once again, the mass loss does not enter into the He core during the evolution of the stars.

As for rotating models during H core burning, in the He core burning phase the rotation implies an enhanced mixing of the chemicals and so an increased CO core mass with respect to non-rotating models. However, the different mass loss and the different timescales available for the rotation to act, which diminish with the initial mass of the star, make the increase of the CO core mass very different between the $30\,M_\odot$ and the $60\,M_\odot$ rotating models. For the first one the increase is $\sim$ 137% while for the second is just $\sim$ 1.3%. It is worth noticing that the two rotating models have an almost identical CO core mass at He depletion, so the mass loss of the heavier one was so efficient that the model resembles a star with half of its initial mass. Regarding the difference between the $60\,M_\odot$ star and the same model with different rate for the reaction (1.4), the CO core mass at He depletion is slightly smaller for the second one: about 0.4%.

After core He depletion, the CO core begins to contract in order to ignite the following nuclear fuel, while the He burning shifts in a shell and drives the formation of a convective zone just above the He burning shell.

1.5 Advanced Nuclear Burning Stages

The nuclear burning stages that follow the H and the He ones, i.e. C-, Ne-, O- and Si-burning, are the so called advanced burning stages. An important aspect of the evolution of massive stars during this phase is the loss of neutrinos. When there is a very high temperature ($\gtrsim 8 \cdot 10^8\,K$) there are enough energetic photons in the Planck distribution with energies in excess that the creation of electron-positron pair is activated. These pairs usually quickly recombine giving back two photons, but a small fraction results in neutrino-antineutrino pairs. The neutrinos, as their opacity in this physical condition is very low, exit the star without interacting with matter and hence they are an efficient energy loss mechanism. The neutrino emission from pair production becomes important roughly at the beginning of the C burning and increases along the following burning phases until the onset of the iron core collapse. So the advanced evolutionary phases of massive stars are referred to as neutrino dominated phases. Due to neutrinos loss the total luminosity of the star undergoes a dramatic increase and since the nuclear energy provided by the burning stages is almost constant there is a severe acceleration of the stellar evolution. Due to this latter being so fast, the surface evolution can not keep the same pace as the core one and so the evolution of the envelope is disconnect from interior one.

The most important parameters that control the evolutionary properties of a massive star after the He depletion are the CO core mass and the $^{12}C/^{16}O$ ratio. The first one determines the thermodynamic history of the core while ^{12}C and ^{16}O abundances constitute the fuel for the more advanced burning stages. The ^{12}C mass fraction at He core exhaustion increases with the mass loss and depends also on the treatment of convection during core He burning and the value of the $^{12}C(\alpha,\gamma)^{16}O$ cross section, which unfortunately are two of the major uncertainties in the computation of massive star models.

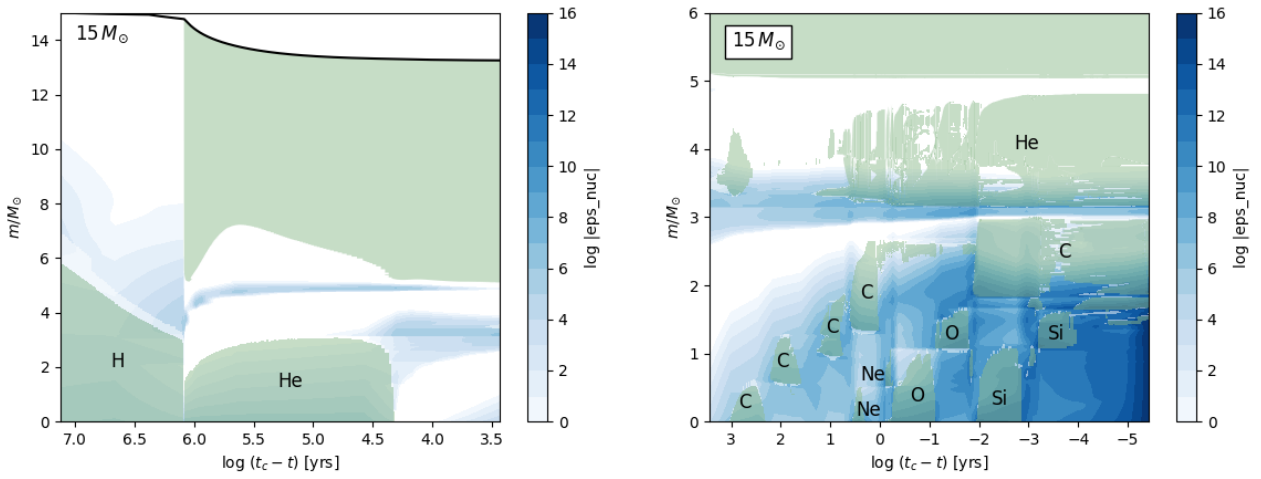

Figure 1.8: Kippenhahn diagram of a 15 $M_\odot$, $Z = 0.014$ star with convective regions (pale green) and nuclear energy generation rate ϵ_{nuc} (blue shades as coded in the color bar) during H and He burning (left) and advanced stages in the inner 6 $M_\odot$ (right). In the x axis there is the logarithm of the time remaining until the onset of core collapse.

1.5.1 C burning

Generally all burning stages begin at the center and form a convective core, which increases in mass and then disappears, after reaching a maximum, as the nuclear fuel is exhausted. The C burning is the only exception: for stars with $M \gtrsim 20\,M_\odot$ it occurs in a radiative environment due to the low ^{12}C mass fraction left by the He core burning coupled to the strong neutrinos loss, which make it impossible to generate a photon luminosity high enough in order to produce a convective core. An example of star that does burn carbon in a convective core is the 15 $M_\odot$ model with solar metallicity $Z = 0.014$ in Fig. 1.8, whereas an example of star that burns C radiatively is the 30 $M_\odot$ model, with same metallicity, in Fig. 1.9.

The main nuclear reaction during this phase is the fusion of two ^{12}C nuclei:

$$^{12}\mathrm{C} + {}^{12}\mathrm{C} \rightarrow {}^{24}\mathrm{Mg}^{*3} \rightarrow {}^{23}\mathrm{Mg} + n \tag{1.12}$$

$$\rightarrow {}^{20}\mathrm{Ne} + \alpha \tag{1.13}$$

$$\rightarrow {}^{23}\mathrm{Na} + p. \tag{1.14}$$

The probability of decay via Eq. (1.13) and Eq. (1.14) is almost the same, while for Eq. (1.12) the probability is smaller, at most 5.4% if $T \sim 5 \cdot 10^9\,K$, since it depends on the temperature. The most abundant elements at the end of C core burning are ^{16}O, from He burning, ^{20}Ne (and two other Ne isotopes), ^{23}Na and ^{24}Mg (and two other Mg isotopes). The lifetimes of the C burning is a few hundred years, but this latter depends on the convection and the $^{12}\mathrm{C}(\alpha,\gamma)^{16}\mathrm{O}$ rate; which defines the ^{12}C abundance at the onset of C burning and thus determines both the size of the core and the

[3] this indicates an excited nucleus

duration of the burning phase.

Once the nuclear fuel is exhausted at the center the burning shifts in a shell which in general induces the formation of a convective zone above it. After the nuclear fuel is depleted within the whole convective zone the burning shell shifts outward in mass and settles where the main fuel is still abundant; then, eventually, another convective zone may form. The number of convective zones formed in each burning stage and their overlap, depends on the mass of the CO core and its chemical composition. Usually there are one to four carbon convective shells and two to three for the neon, oxygen and silicon burning. For instance the $15\,M_\odot$ with $Z = 0.014$ develops four carbon shells and one for neon, oxygen and silicon (Fig. 1.8). In general, the number of C convective shells increases as the mass of the CO core decreases.

1.5.2 Ne burning

Among ^{16}O, ^{20}Ne and ^{24}Mg, which are the most abundant elements at the onset of neon (Ne) burning, the first one has the smallest Coulomb barrier, but before the oxygen (O) burning sets in there is the partial photodisintegration of the ^{20}Ne, being this the most fragile nucleus among them. The photodisintegration and α-capture reactions in the Ne burning can be written in a combined way as:

$$2\,^{20}\mathrm{Ne} \rightarrow {}^{16}\mathrm{O} + {}^{24}\mathrm{Mg}. \tag{1.15}$$

Neon burning occurs in a convective core independently of the initial mass of the massive star (if above a mass threshold around $\sim 11\,M_\odot$); due to energy loss by neutrinos streaming this burning phase is very short and lasts a few months or at most a year while depending on convection, like the C burning. At the end of Ne burning the so called oxygen-magnesium core is mainly composed of ^{16}O and various isotopes of ^{24}Mg, ^{26}Al, ^{28}Si and ^{30}P. After neon depletion in the stellar core, the Ne burning shifts to a shell, but since the O burning starts so soon there is not enough time for a significant Ne burning shell phase. In fact, e.g. in Fig. 1.8 and 1.9the neon shell is barely visible around $log(t_c - t) \sim 0$.

1.5.3 O burning

Oxygen burning is similar to the C burning since, when the burning occurs through oxygen fusion, even here an unstable nucleus is formed which then decays producing different elements. In the O burning there are four channels:

$$\begin{aligned} {}^{16}\mathrm{O} + {}^{16}\mathrm{O} \rightarrow {}^{32}\mathrm{S}^* &\rightarrow {}^{31}\mathrm{S} + n && (1.16)\\ &\rightarrow {}^{31}\mathrm{P} + p && (1.17)\\ &\rightarrow {}^{30}\mathrm{P} + d && (1.18)\\ &\rightarrow {}^{28}\mathrm{Si} + \alpha. && (1.19) \end{aligned}$$

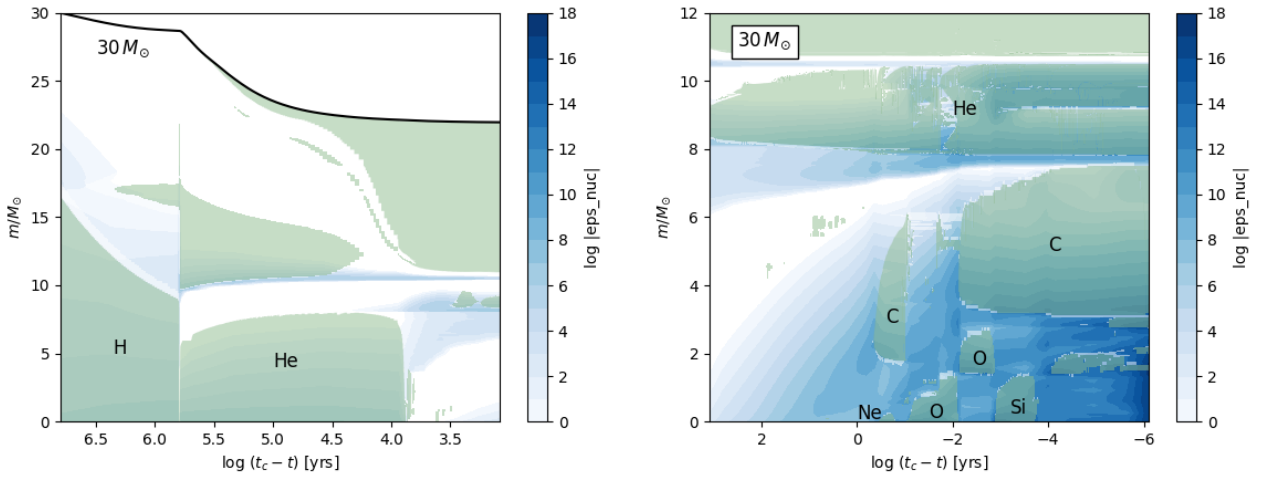

Figure 1.9: Same as in Fig. 1.8 but for a 30 $M_\odot$ star with metallicity $Z = 0.014$.

The probability of the various reactions (1.9-1.12) are 5%, 56%, 5% and 34% respectively. The third one is allowed only at high temperatures, and then the deuterium is photodisintegrated into a proton and a neutron, while for lower temperatures is inhibited. Hence at lower temperatures there are only three channels for the oxygen fusion. O burning occurs in a convective core as well and lasts a bit longer than the Ne burning. This behavior is due to the very high oxygen mass fraction at the onset of this burning phase and the bigger energy gain with respect of that of Ne burning. At oxygen depletion almost 90% of the final composition is constituted of ^{28}Si and ^{32}S, so the O burning produces a silicon-sulfur core. After the core burning one or more O burning shells outside the oxygen depleted core are formed.

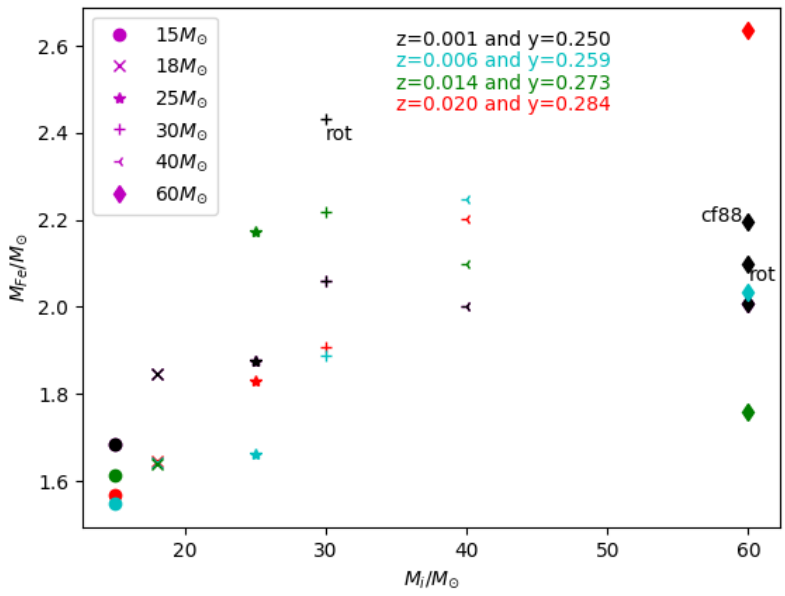

Figure 1.10: Iron core mass, at Si depletion, for all the models as function of the initial mass and for the four metallicities as indicated.

1.5.4 Si burning

Unlike the two previous major burning stages, carbon and oxygen, silicon (Si) burning does not occur as a fusion process due to prohibitively high Coulomb barrier for the reaction $^{28}\mathrm{Si}+^{28}\mathrm{Si} \rightarrow {}^{56}\mathrm{Ni}$. Instead, silicon burns through a series of photodisintegration and α-capture reactions. The first ones produce α particles (^{4}He) which are then captured by other nuclei to form heavier elements:

$$^{28}\mathrm{Si}(\gamma,\alpha)^{24}\mathrm{Mg}(\gamma,\alpha)^{20}\mathrm{Ne}(\gamma,\alpha)^{16}\mathrm{O}(\gamma,\alpha)^{12}\mathrm{C}(\gamma,\alpha)2\alpha \tag{1.20}$$

$$^{28}\mathrm{Si}(\alpha,\gamma)^{32}\mathrm{S}(\alpha,\gamma)^{36}\mathrm{Ar}(\alpha,\gamma)^{40}\mathrm{Ca}(\alpha,\gamma)^{44}\mathrm{Ti}(\alpha,\gamma)\cdots{}^{56}\mathrm{Ni}. \tag{1.21}$$

Silicon burning, as mentioned at the beginning of this chapter, occurs in a convective core and it is extremely short, $\sim 10^{-2}\,yr$; the core composition after this burning stage is mainly ^{56}Fe and ^{52}Cr and like for previous nuclear fuels, the star undergoes one or more shell-burning episodes (e.g. Fig. 1.8 and 1.9) which have great impact on the stellar structure at the onset of the iron core collapse. Figure 1.10 shows the iron (Fe) core mass at Si depletion for all the models as function of the initial mass of the star. It is worth noting that both rotation and the different rate for the $^{12}\mathrm{C}(\alpha,\gamma)^{16}\mathrm{O}$ reaction increase the Fe core mass. In Table 1.2 are listed the exact values for the $60\,M_\odot$ $Z = 0.001$ model with and without rotation and with the different rate and also for the same models with initial mass $30\,M_\odot$. The different rate means an increase of the Fe core mass equal to $\sim$ 9.5%, while the inclusion of rotation increases the value about $\sim$ 4.6% and $\sim$ 18% for the $60\,M_\odot$ model and $30\,M_\odot$ model respectively. It is very likely that the fact that the rotating models experience such different mass losses during their evolution is the reason why the $60\,M_\odot$ model has a smaller increase in the Fe core mass with respect to the $30\,M_\odot$ one.

1.6 Evolution of surface abundances

In Fig. 1.11 there are the surface abundances, as function of time, of the models with $30\,M_\odot$ and

$60\,M_\odot$ with initial composition $Z = 0.001$ and $Y = 0.250$ and the corresponding rotating models 30.rot and 60.rot. As can be seen, for the non-rotating models the abundances are quite constant throughout the whole evolution, while for the other two the surface composition changes a lot. This is due to the interplay of two factors: the rotation, and hence the enhanced mixing inside the star, and the increased mass loss. It is worth noting that already during the MS phase both rotating models have enhanced N surface abundances while C and O decrease and then rise during the advanced stages of the evolution. The composition changes driven by both factors, together with the evolution towards high effective temperatures, lead the models to get the physical characteristics of a WR star. As showed already in Fig. 1.2 the 30.rot and 60.rot enter the WNL phase early on in their evolution during the H burning phase, at $\sim 6.9\cdot10^6\,yr$ and $\sim 3.4\cdot10^6\,yr$ respectively as the hydrogen surface abundance is $X_H < 0.4$. The WC phase starts at $\sim 9.2\cdot10^6\,yr$ for the $30\,M_\odot$ model and at $\sim 5\cdot10^6\,yr$ for the $60\,M_\odot$ one, when C, He and O become the most abundant elements at the surface.

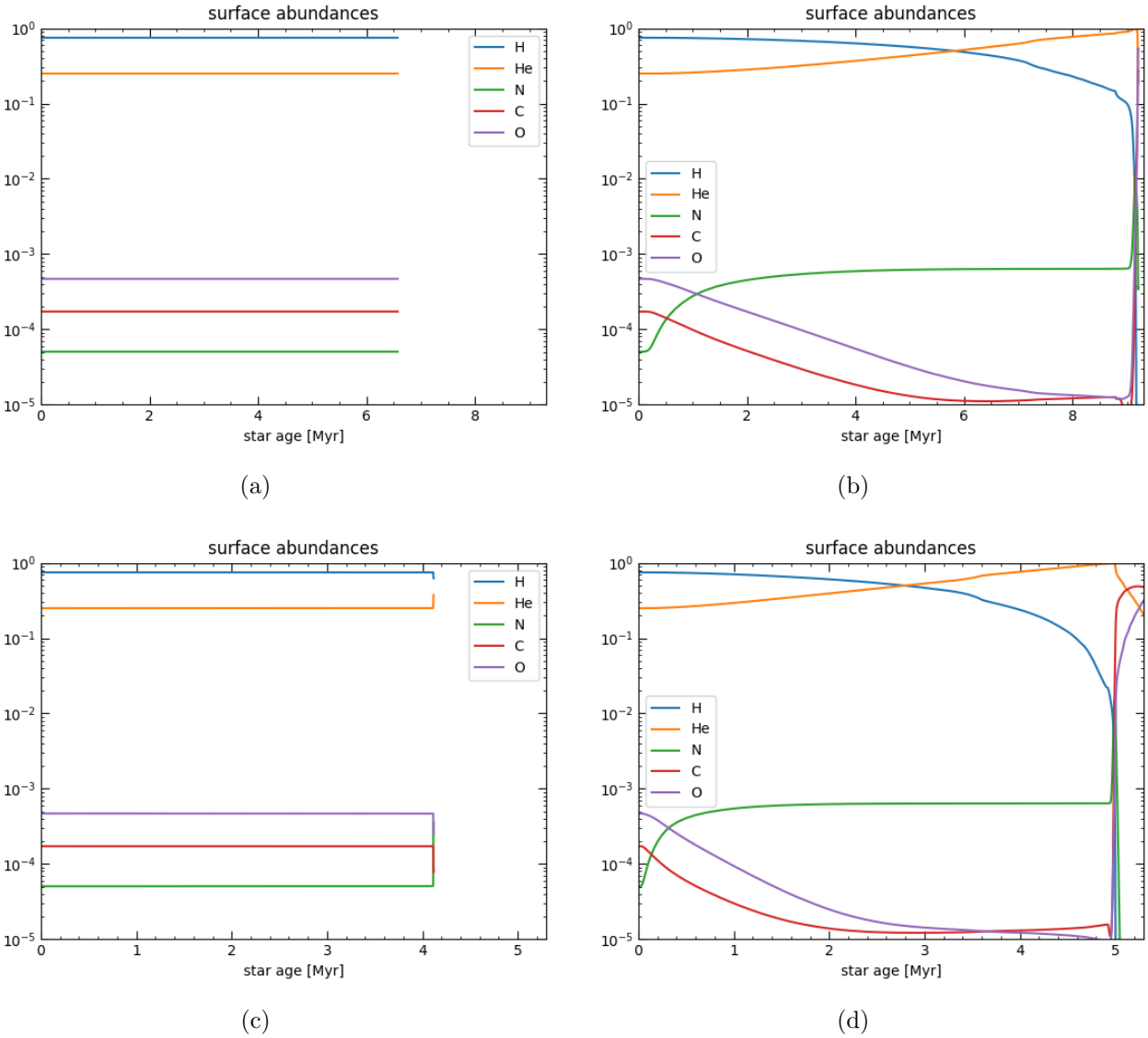

Figure 1.11: surface abundances of the principle elements as function of star age. In the four panels there are the 30 $M_\odot$, the 30.rot, the 60 $M_\odot$ and the 60.rot models respectively, all with the same initial composition (see Table 1.1).

1.7 Presupernova Stage

The interplay between all the shell nuclear burnings and the overlap of the convective zones determines the mass-radius relation of the star and its chemical stratification at the presupernova stage. The less efficient the C burning shell, i.e. the lower the ^{12}C mass fraction left by core He burning, the fewer the convective zones the higher the contraction of the CO core and the steeper the final mass-radius relation i.e. the compactness. This means that for higher CO core mass the structure of the star is expected to be more compact.

Figure 1.12 shows the abundances of a few nuclear species at the presupernova stage for four models with initial mass of 60 $M_\odot$ and metallicity $Z = 0.001$, $Z = 0.006$, $Z = 0.014$ and $Z = 0.02$ respectively. Going through the four plots one can easily see that with the increasing metallicity the H-rich envelope and the He core are progressively reduced by the mass loss. At this point, i.e. presupernova stage, the star consists of an iron core, with mass between $\sim$ 1.5 $M_\odot$ and $\sim$ 2.6 $M_\odot$ (Fig.

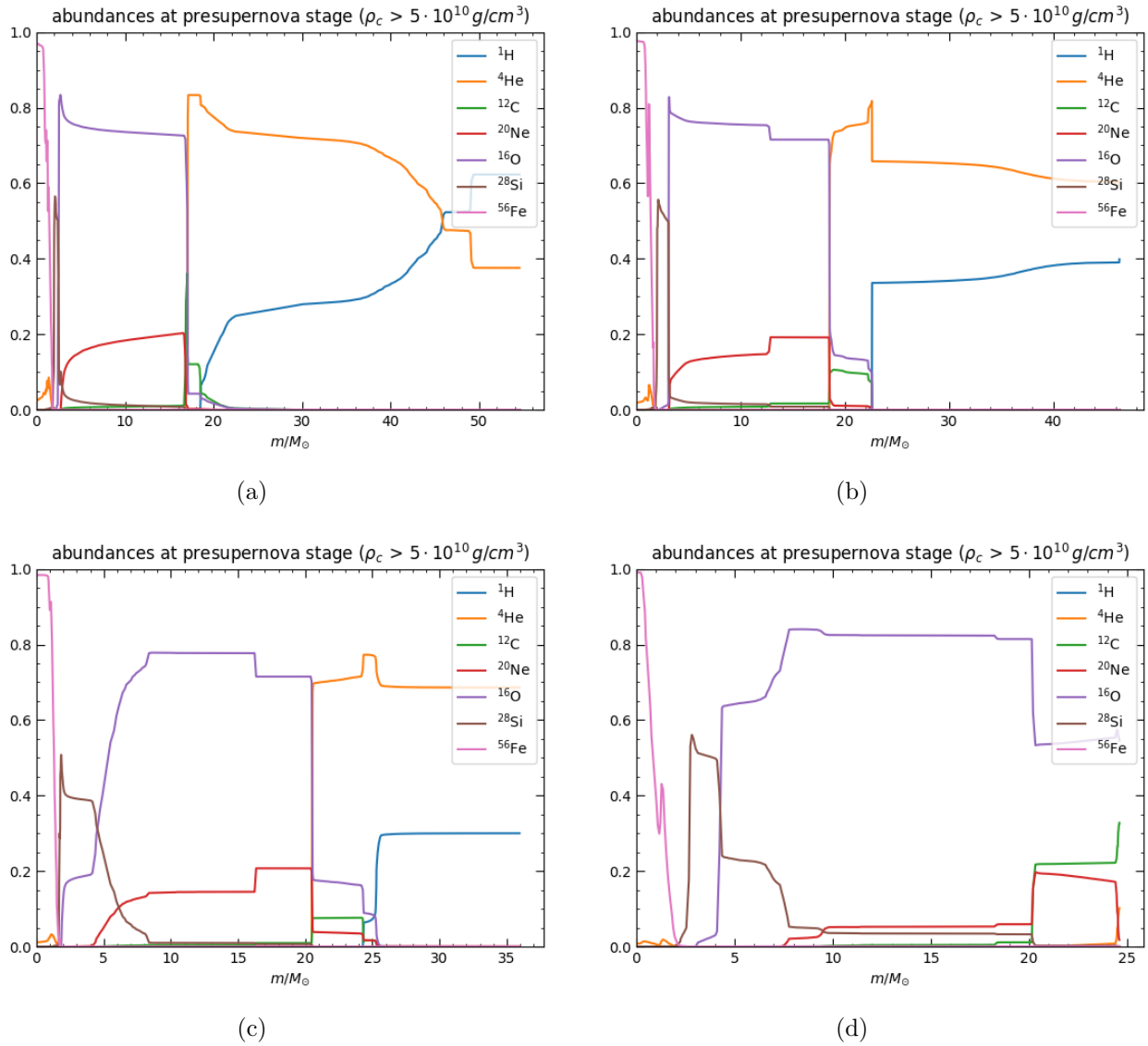

Figure 1.12: Internal distribution of the principle elements at presupernova stage for stars with 60 $M_\odot$ and different metallicity.

1.10 and Table 1.3), which is surrounded by active burning shells at the base of the various regions composed by the main products of the stable core burnings, i.e. the onion-skin structure.

Table 1.3: values of M_{ZAMS}, M_{pre-SN} and M_{Fe} for all the models subdivided according to the initial metallicity.

	M_{ZAMS} $[M_\odot]$	M_{pre-SN} $[M_\odot]$	M_{Fe} $[M_\odot]$
$Z = 0.001$			
	15	14.742	1.686
	18	17.748	1.845
	25	24.526	1.874
	30	29.452	2.060
rot	30	17.773	2.432
	40	38.647	2.002
	60	54.548	2.007
rot	60	17.658	2.100
cf88	60	54.594	2.197
$Z = 0.006$			
	15	13.773	1.547
	18	16.498	1.641
	25	23.572	1.660
	30	26.409	1.887
	40	28.714	2.249
	60	46.366	2.034
$Z = 0.014$			
	15	13.234	1.612
	18	16.707	1.638
	25	18.992	2.173
	30	21.929	2.219
	40	26.217	2.099
	60	35.951	1.760
$Z = 0.02$			
	15	13.193	1.568
	18	16.482	1.646
	25	19.300	1.830
	30	17.882	1.906
	40	24.399	2.201
	60	24.612	2.634

Chapter 2

The Explodability of Massive Stars

Presupernova stars show large variation of their structural properties with respect to the M_{Fe}, the binding energies, the density and entropy profiles. These properties have a non-monotonic behavior with respect to the initial mass of the star likewise the properties of neutrino-driven supernovae like explosion energy, nickel mass and remnant mass are strongly non-monotonic (Ugliano et al. 2012). In this chapter after a section dedicated to the neutrino-driven mechanism of the SN explosion, I provide a brief overview of two different explodability criteria based on the compactness parameter, ξ_M, and the M_4-μ_4 parameters, respectively.

2.1 Neutrino Driven Explosion

From the onset of the core collapse to the initiation of the SN explosion the evolution can be divided into six stages (Janka 2017): gravitational instability and collapse of the stellar core, core bounce and shock formation, shock stagnation and shock-breakout neutrino burst, neutrino heating and accretion, shock revival and finally explosion and nucleosynthesis.

The gravitational instability of the degenerate iron core is initiated by electron captures on nuclei and free protons, which produce electron neutrinos ν_e and partial photodisintegration of heavy nuclei into α particles and free nucleons. Both effects lead to a reduction of the adiabatic index of the equation of state below the critical value of 4/3. At density $\sim 10^{11}\, g/cm^3$ the neutrino mean free path becomes so short that neutrinos begin to interact with stellar matter and diffuse while in an environment with lower density they can escape easily. Then, at density $\sim 10^{12}\, g/cm^3$, the neutrino diffusion is slower than the accelerating infall of the plasma and neutrino trapping starts to set in. The subsonically collapsing inner core develops a homologous velocity profile with a maximum nearly free-falling supersonic velocity near the edge between the inner core and the outer core.

In the second stage the implosion of the inner core is halted when at the center the nuclear saturation density $\sim 2.7 \cdot 10^{14}\, g/cm^3$ is reached, which leads to a stiffening of the equation of state. Now a new stable state sets in in which stellar matter is supported against gravity by its own pressure. This matter is incompressible due to the repulsive strong nuclear force that acts between nucleons. The inner core bounces back creating pressure waves that steepen into a shock front at the transition with the supersonically infalling outer core, roughly speaking at $\sim 0.5\, M_\odot$ in mass coordinate.

At the beginning of the shock stagnation and shock-breakout neutrino burst stage, the shock starts to propagate outwards. This causes a dissipation of kinetic energy in the infalling matter and hence creates high-energy photons that lead to photodisintegration of the iron nuclei to free nucleons. The photodisintegration drains $1.7 \cdot 10^{51}\, erg$ per $0.1\, M_{\odot}$ of energy reducing the post-shock pressure. After having overrun only $\sim 0.5\, M_{\odot}$ of iron-core matter, the bounce shock stops while being still inside the collapsing iron core. The density behind the shock decreases and, as a consequence, electron neutrinos, produced by electron captures onto free protons, start to escape freely. In the so called shock-breakout neutrino burst a great amount of neutrinos are radiated away and this steals even more energy from the post-shock layer so that the shock expansion stalls.

At later post-bounce times the post-shock temperature decreases as the density drops and the plasma begins to be more radiation dominated, while the neutrino spectra radiated from the NS harden. The radiation domination diminishes the neutrino cooling and the higher energetic neutrinos make it possible for neutrons and protons to reabsorb a great fraction of them. This marks the beginning of the neutrino heating phase, in which the stalled shock receives energy from the neutrinos. The heated layer can become convectively unstable and the accretion shock instability can grow in the mass-accretion flow between shock and nascent NS.

Contrarily to earlier photodisintegration, the neutrino-energy transfer to the shock raises the post-shock pressure and, if the heating is strong enough, the shock can be pushed outwards, the explosion can be launched. Due to non-radial fluid instabilities, the layer of neutrino-energy deposition grows and neutrino-heated matter moves outwards to the shock while cooler gas goes towards the NS where it can be heating more efficiently. For these massive stars the high mass-accretion rate of the core has two opposite effects. A higher mass accretion rate obstructs the expansion of the stalled shock, because it has to be overcome by the post shock pressure. Hence this latter needs to be bigger in order to start the outward shock expansion. Moreover, a high mass accretion rate also increases the total luminosity of electron neutrinos and antineutrinos (Janka 2017):

$$L_{\nu_e} + L_{\bar{\nu}_e} \sim 2L_{\nu_x} + \frac{GM\dot{M}}{R_{NS}}, \tag{2.1}$$

The first term on the right hand side (rhs) represents the contribution of neutrinos exiting from the core of the NS in terms of the luminosity of one species of heavy lepton neutrinos. The other term is the accretion component L_{ν}^{acc}: energy radiated by electron neutrinos and antineutrinos produced by the matter inflow at the NS radius. Depending on which one of theses two effects prevail the explosion will be launched successfully or not. So, if the thermal pressure behind the shock overcomes the ram pressure of the infalling pre-shock layer, runaway shock expansion can set in. The acceleration of the shock triggers explosive nucleosynthesis, producing radioactive iron-group and intermediate-mass nuclei, which power the SN light curve.

During the final stage there is a phase of simultaneous mass accretion and outflow towards and from the NS and when it ends the so called neutrino-driven wind is launched by the NS: an outflow of free neutrons and protons from its surface. These recombine to α particles and partly to heavy nuclei. Due to this neutrino-driven wind nucleosynthetic yields can be added to the innermost SN ejecta. The shock needs hours or even a day to reach the stellar surface, meanwhile the compact remnant cools and deleptonizes by neutrino and antineutrino radiation.

2.2 Mono-parametric criterion: $\xi_{2.5}$

O'Connor & Ott (2011) use their open-source general-relativistic 1.5D code *GR1D* to study over 100 presupernova models from Woosley & Weaver (1995), Woosley et al. (2002), Limongi & Chieffi (2006) and Woosley & Heger (2007). They find that post-bounce evolution and the outcome of a stellar model can be estimated in a good approximation by the compactness of the star. They define the bounce compactness $\xi_{2.5}$ as:

$$\xi_M = \frac{M/M_\odot}{R(M_{bary} = M)/1000\,km}\bigg|_{t=t_{bounce}}, \tag{2.2}$$

where M is set to $2.5\,M_\odot$ and $R(M_{bary} = 2.5\,M_\odot)$ is the radius that encloses the chosen mass at bounce time. The $2.5\,M_\odot$ mass was chosen since it is the relevant mass scale for BH formation. As they discuss in their article the post bounce time to black hole formation, which is the upper limit time available for the neutrinos to reenergize the stalled shock and launch the explosion, can be written as a function of this parameter as $t_{BH} \propto (\xi_{2.5})^{-3/2}$ (see O'Connor & Ott for details). Hence, very roughly speaking, the more compact the star is the faster a BH will be produced from the proto-neutron star (PNS) and thus the mechanism responsible for the actual launch of the explosion has less time available in order to do that. This implies a more likely failure of the core collapse SN (CCSN) explosion.

Another useful quantity in the analysis done by O'Connor and Ott is the time-averaged heating efficiency of the critical model $\bar{\eta}^{crit}_{heat}$. It specifies how much energy from the neutrino luminosity must be deposited on average, between the bounce time and the explosion time, in order to make a stellar model explode. They divide their models in the $\xi_{2.5}-\bar{\eta}^{crit}_{heat}$ plane in two regimes: those with $\xi_{2.5} \lesssim 0.45$ and those with $\xi_{2.5} \gtrsim 0.45$. For the former set the explosion is the most probable outcome since it is needed a roughly constant and not so high value of $\bar{\eta}^{crit}_{heat}$ in order to the neutrino mechanism to be successful (assuming stiffness of the EOS similar to those in the aforementioned article). As to the latter set of models their fate is likely the formation of a BH due to very high heating efficiency, which increases with $\xi_{2.5}$, required to drive an explosion. The threshold at $\xi_{2.5} \sim 0.45$ divides models that do produce a SN explosion from those that form a BH.

The compactness parameter is defined in Eq. (3.2) at the stage of core bounce. Under the reasonable assumption that $\xi_{2.5}$ does not change appreciably during the collapse (Limongi 2017), I opted to evaluate and check the parameter when the central density $\rho_c = 5 \cdot 10^{10}\,g/cm^3$ for all my models. The choice of the density value ensures physical conditions consistent with those adopted to test the other explodability criteria (see Sect. 2.3).

Fig. 2.1 shows the values of compactness parameter $\xi_{2.5}$ for all the stellar models organized as function of the metallicity Z. Following the compactness criterion there are 9 stellar models that produce a SN explosion (see those in red in Fig. 2.1). All progenitors with $M \geq 30\,M_\odot$ are not expected to revive the stalled shock and hence they fail to explode and produce a BH. The only exception is the $60\,M_\odot$ model with $Z = 0.014$ that has a compactness value of $\xi_{2.5} = 0.369$.

Table 2.1: values of M_{ZAMS} and $\xi_{2.5}$ for all the models subdivided according to the initial metallicity.

	M_{ZAMS} $[M_\odot]$	$\xi_{2.5}$
$Z = 0.001$		
	15	0.366
	18	0.980
	25	0.798
	30	0.530
rot	30	1.567
	40	0.937
	60	1.740
rot	60	1.554
cf88	60	0.589
$Z = 0.006$		
	15	0.081
	18	0.361
	25	0.337
	30	0.562
	40	1.153
	60	1.205
$Z = 0.014$		
	15	0.287
	18	0.219
	25	1.064
	30	2.190
	40	1.047
	60	0.369
$Z = 0.02$		
	15	0.108
	18	0.225
	25	0.999
	30	0.757
	40	1.728
	60	3.027

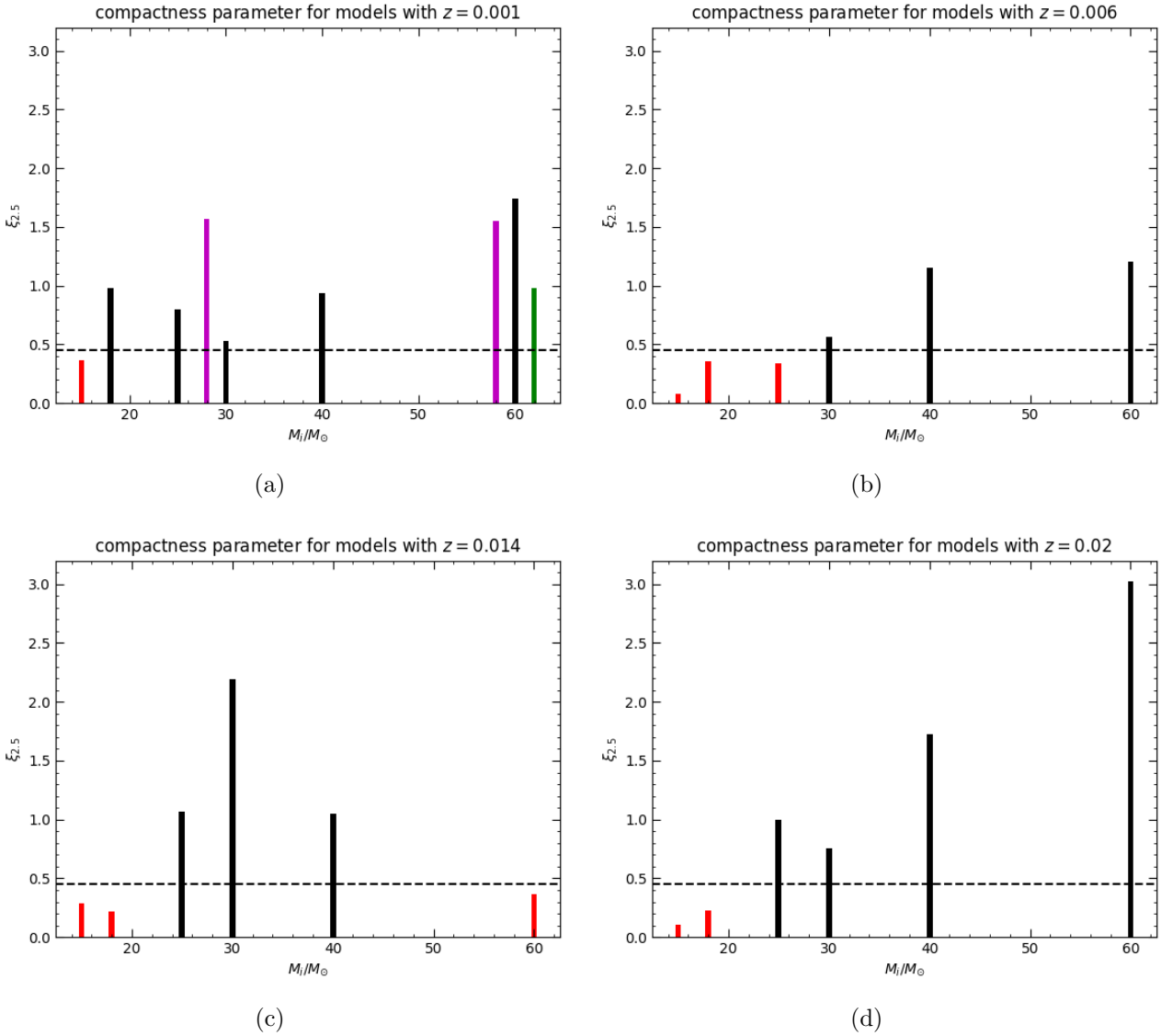

Figure 2.1: Compactness parameter $\xi_{2.5}$ as function of the initial mass for all models and metallicities. The horizontal dashed line represents the threshold value for the compactness (see text). In red the models that explode while in black those that produce a BH. The magenta bars indicate the two rotating models with initial mass $30\,M_\odot$ and $60\,M_\odot$ respectively, while the green bar indicates the $60\,M_\odot$ model with the test rate for the reaction $^{12}\mathrm{C}(\alpha,\gamma)^{16}\mathrm{O}$.

2.3 Bi-parametric criterion: M_4-μ_4

Ertl. et al (2016) investigate over 600 stellar models from Woosley et al. (2002), Woosley et al. (2007), Sukhbold & Woosley (2014) and Nomoto et al. (2006), by performing collapse and explosion simulations. For the calibration of the core-model parameters they choose 5 different progenitors with initial mass between 15 and 20 $M_\odot$ in order to reproduce the explosion energy and the ejected ^{56}Ni mass of SN1987A (model s19.8 of Woosley et al. 2002, model w15.0 of Woosley et al. 1988, model w18.0 of Woosley et al. 2007, model w20.0 of Woosley et al. 1997 and model n20.0 of Shigeyama & Nomoto 1990).

Ertl et al. state that in the case of the compactness parameter $\xi_{2.5}$ the threshold for BH formation grows with the initial mass of the star and therefore it cannot be assigned a single value, as suggested by O'Connor & Ott (2011). For this reason Ertl et al. claim that a second parameter, e.g. $\xi_{1.5}$, the iron core mass M_{Fe}, the binding energy E_b outside M_{Fe}, may provide a more realistic description. Under these leading hypothesis, the authors carried out a systematic investigation of the large grid of models they computed in the framework of the neutrino-driven explosion (see Sect. 2.1).

They found that if the neutrino luminosity grows above a critical value $L_{\nu,crit}(\dot{M})$ then the propagation of the shock takes place and the explosion is eventually triggered. During this phase the proto-neutron star (PNS) acts as accretor and the value of its mass M_{NS} can be substituted by $M = m(r)$: the enclosed mass of the progenitor structure which remains locked at the onset of the explosion (mass cut). Then, a measure of the mass accretion rate could be $\dot{M} \propto m'(r) = dm/dr$ and so the two parameters $M = m(r)$ and $\dot{M} \propto m'(r)$ could classify the explodability of the progenitors. The last statement can be justified by the following reasoning: the accretion component of the rhs of Eq. (2.1) can be rewritten as $L_\nu^{acc} \propto GM_{NS}\dot{M} \propto Mm'(r)$, given that the dependence on R_{NS} can be neglected, (see Sect. 3.6 of Ertl et al. (2016) for details on why the neutrino luminosity dependence on the NS radius is not so fundamental) and since it accounts for the major component of the neutrino luminosity of the PNS this latter becomes $L_\nu \propto L_\nu^{acc} \propto Mm'(r)$. Ertl et al. show that there is a correspondence between the $L_\nu - \dot{M}$ plane and the $Mm' - m'$ parameter plane. According to their simulations the onset of the explosion coincides approximately with the moment when infalling matter with entropy per nucleon $s \sim 4$ reaches the shock. Therefor, the mass parameter M_4, defined as:

$$M_4 = m(s = 4)/M_\odot, \tag{2.3}$$

can be taken as a proxy of the PNS mass, and the parameter μ_4, defined with:

$$\mu_4 = \left.\frac{dm/M_\odot}{dr/1000\,km}\right|_{s=4} = \left.\frac{\Delta m/M_\odot}{\Delta r/1000\,km}\right|_{s=4} = \tag{2.4}$$

$$= \frac{(M_4 + \Delta m/M_\odot) - M_4}{[r(M_4 + \Delta m/M_\odot) - r(s = 4)]/1000\,km}, \tag{2.5}$$

can be reasonably taken as a measure of the mass accretion rate.

This is evaluated as the average mass gradient outside $s = 4$ with $\Delta m = 0.3\,M_\odot$, since this mass interval yields the best results in Ertl et al (2016). Identified M_4 and μ_4 as suitable parameters, the

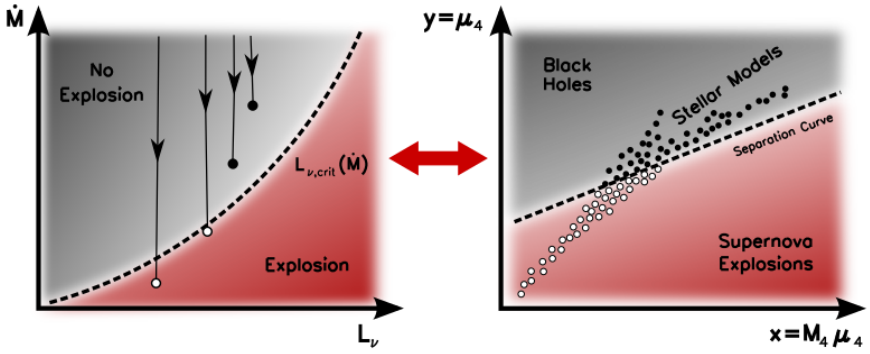

Figure 2.2: Figure 6 from Ertl et al. (2016). On the left there is the $L_\nu - \dot{M}$ plane with the critical neutrino luminosity $L_{\nu,crit}(\dot{M})$, while on the right there is the correspondent parameter plane $M_4\mu_4 - \mu_4$ with the separation curve given by Eq. (3.6). In the left plot there are four examples of post bounce evolution path: two that launch an explosion (white) and two that do not (black). These correspond to white and black circles in the right plot where pre-collapse models are represented.

explodability analysis originally based on the $L_\nu - \dot{M}$ diagram, can be conveniently transferred to the $M_4\mu_4 - \mu_4$ diagram (Fig. 2.2).

The SN explosion region and the BH formation region are defined by the so called separation line represented by the function:

$$y_{sep}(x) = k_1 x + k_2, \tag{2.6}$$

where $x = M_4\mu_4$, $y = \mu_4$ and the two coefficient k_1 and k_2 are computed by minimizing the number of outliers for each of the five calibration models in Ertl et al. (2016). Thus there are five different possible separation lines as can be seen in Fig. 2.3 (see the caption of Fig. 2.3 for details on these 5 separation lines). Since those lines have an inclination, μ_4 depends on $M_4\mu_4$ and this shows that two parameters are necessary in order to better capture the explodability of the models. M_4 and μ_4 are both computed, for all the models, when the central density of the progenitor during its presupernova evolution reaches the value of $\rho_c = 5 \cdot 10^{10}\, g/cm^3$. This value was chosen to maintain the reference density adopted in Ertl et al. (2016), which has the advantage to be still close to the pre-collapse phase so that it better describes the structure of the star before the onset of collapse.

Figure 2.3 displays all the pre-supernova models computed in this study in the $M_4\mu_4 - \mu_4$ diagram. Only the $15\,M_\odot$ star with $Z = 0.006$, the $15\,M_\odot$ model with $Z = 0.02$ and $18\,M_\odot$ star with $Z = 0.014$ do explode according to all five possible separation lines; while the $18\,M_\odot$ model with $Z = 0.02$ and $60\,M_\odot$ star with $Z = 0.001$ may have different outcomes depending on the assumed separation line. All the other models form a BH.

As can be seen, in both the $30\,M_\odot$ and the $60\,M_\odot$ cases adding the rotation shifts the position of the models towards the upper left part of the plane. For the first one the outcome does not change although there is an increase of $\sim$ 380% in the $M_4\mu_4$ parameter and of $\sim$ 365% in the μ_4 one. For the second, instead, there is a much lower difference between the models with and without rotation, about $\sim$ 33% in the x coordinate and $\sim$ 34% in the y coordinate, but the outcome does change: the rotating model produces a BH according to all five different separation lines. Similarly, the differences between the $60\,M_\odot$ $Z = 0.001$ model with the default reaction rate for $^{12}C(\alpha,\gamma)^{16}O$ and the same

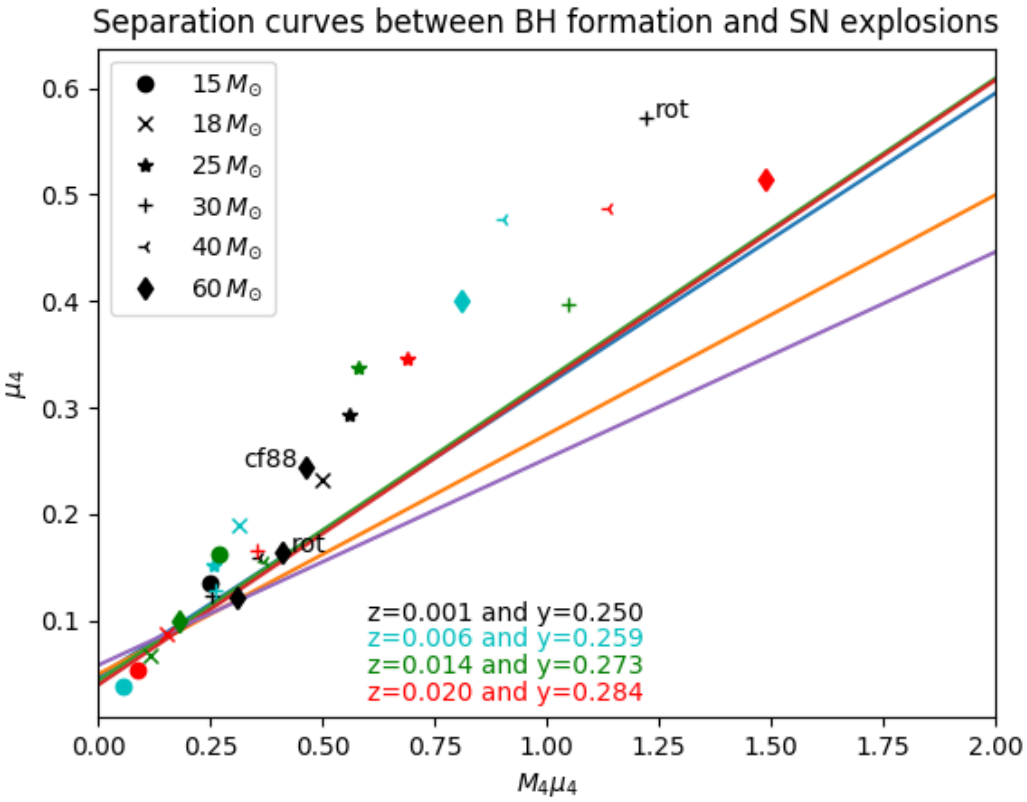

Figure 2.3: Separation curves between BH formation and SN explosions for all the 24 models in the $M_4\mu_4 - \mu_4$ plane. Mass and metallicity of the various stellar models are coded with different symbols and colors as stated in the plot. The colored lines represent five different progenitor models used in Ertl et al. (2016) (see text). The blue one is model s19.8 of the s2002 series of Woosley et al. (2002), in orange w15.0 of Woosley et al. (1988), w18.0 of Woosley et al. (2007) in green, in red w20.0 of Woosley et al. (1997) and the purple one is the n20.0 model of Shigeyama & Nomoto (1990). With 'rot' are indicated those stellar models with initial rotation velocity $\Omega/\Omega_c = 0.7$ where Ω_c is the critical rotation velocity and with 'cf88' is indicated the model with different rate for the reaction $^{12}\mathrm{C}(\alpha,\gamma)^{16}\mathrm{O}$ (see Sect. 3.1.3).

model with a test rate (cf88 in Fig. 2.3) make the latter shift well inside the BH forming region, with an increase in $M_4\mu_4$ of $\sim$ 50% and $\sim$ 100% in μ_4.

As discussed in Sect. 2.1, explosions are favored by the combination of a massive PNS, meaning a high neutrino luminosity, and a low value of the accretion rate, that implies a small ram pressure in the region between the shock and the PNS. Thus high values of M_4 coupled with low values of μ_4 favor the explosion since both the aforementioned conditions are met. This is, for example, the case of the 60 $M_\odot$ model with initial metallicity $Z = 0.001$ (Fig. 2.4a and Fig. 2.5a). In Fig. 2.4 and Fig. 2.5 are plotted respectively the values of parameter M_4 and parameter μ_4 subdivided in function of the initial metallicity of the models.

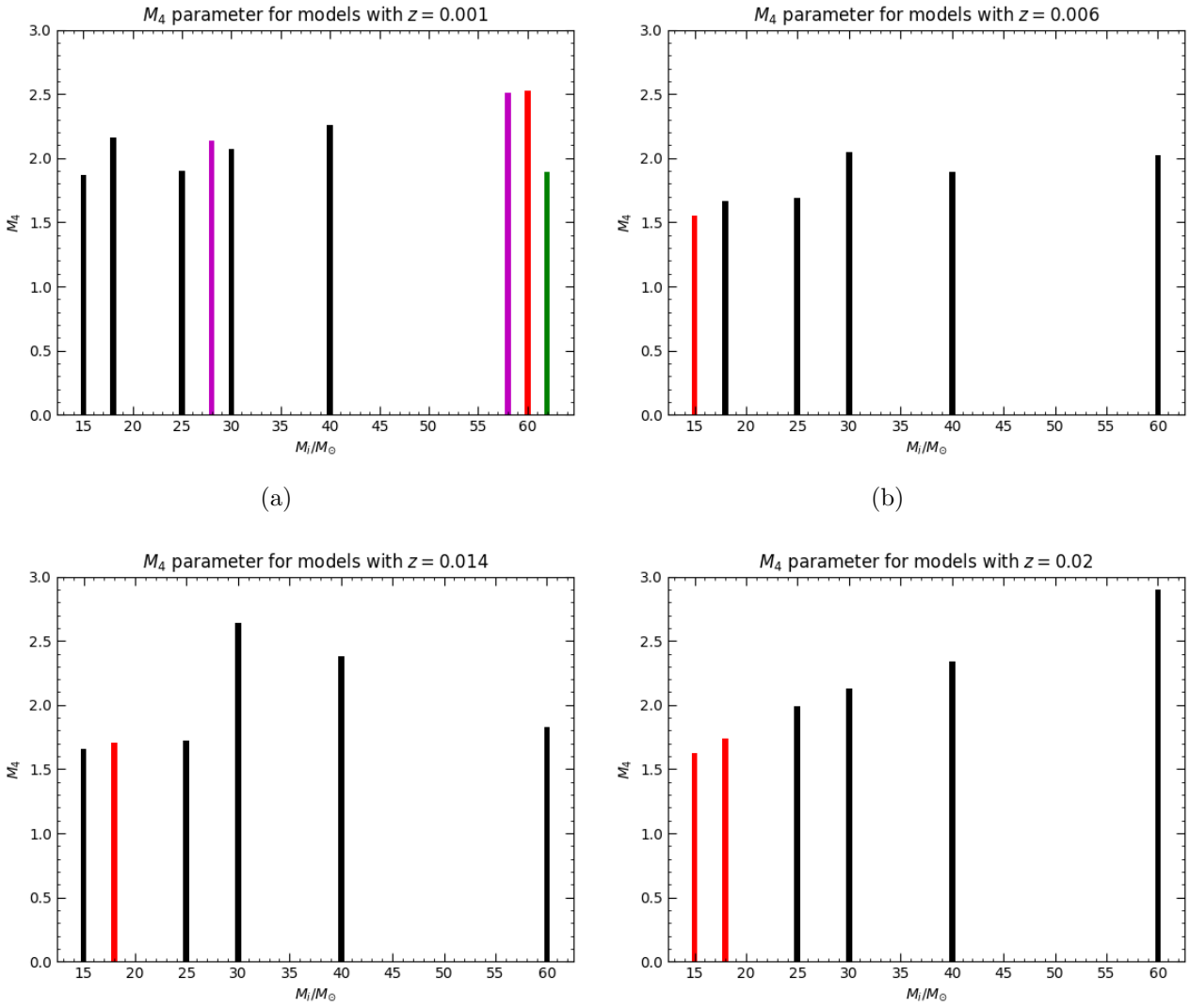

Figure 2.4: M_4 parameter as function of the initial mass for all models metallicities. Red bars indicate models that explode while black bars models that produce a BH. Magenta and green bars have the same meaning as in Fig. 2.1 .

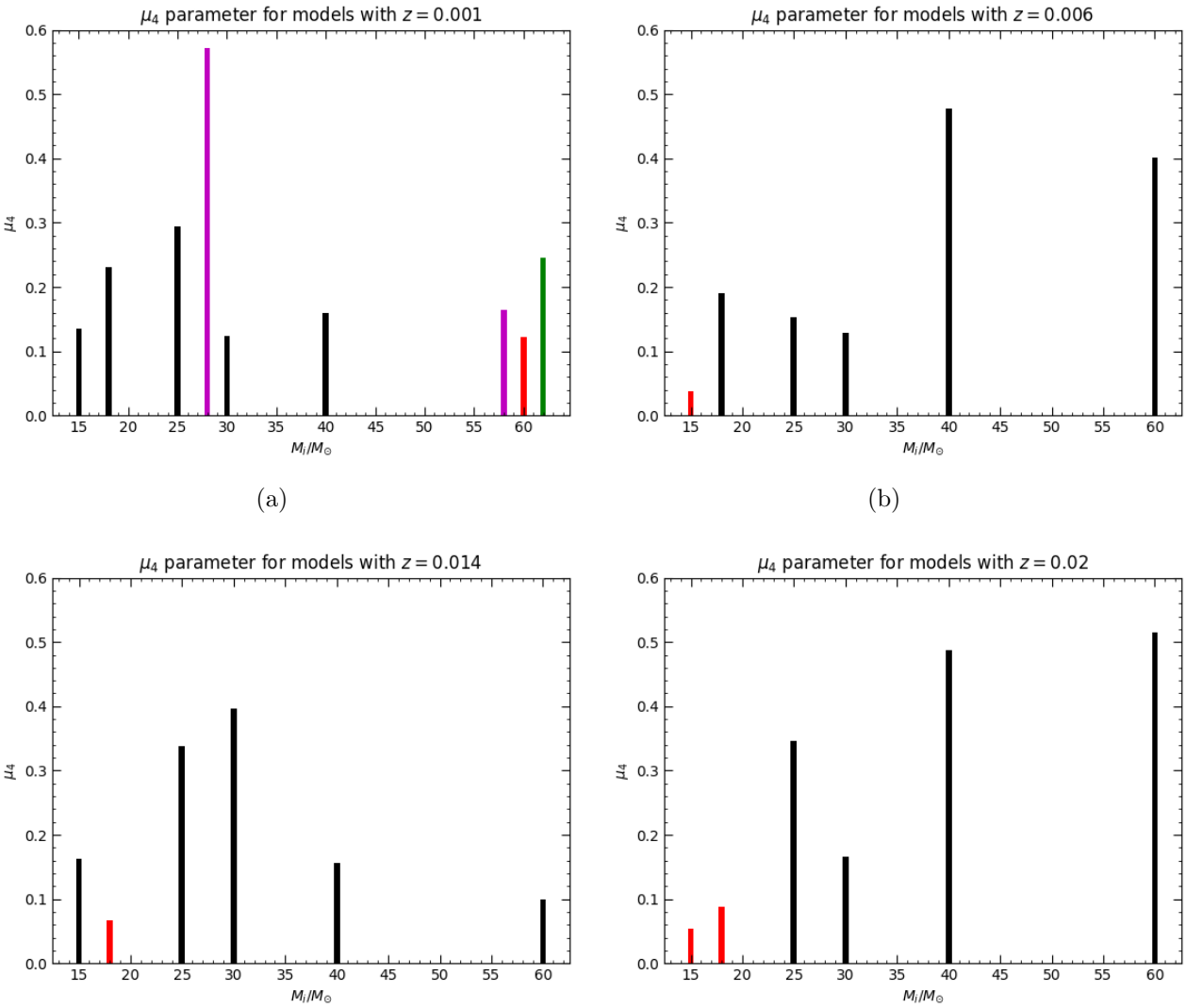

(a) (b)

(c) (d)

Figure 2.5: Same as in Fig. 2.4 for the μ_4 parameter.

Table 2.2: M_4 and μ_4 parameters for all the presented models.

	initial mass $[M_\odot]$	M_4	μ_4
$Z = 0.001$			
	15	1.870	0.135
	18	2.161	0.231
	25	1.903	0.294
	30	2.075	0.123
rot	30	2.136	0.572
	40	2.257	0.160
	60	2.523	0.122
rot	60	2.509	0.164
cf88	60	1.895	0.245
$Z = 0.006$			
	15	1.549	0.038
	18	1.668	0.189
	25	1.688	0.152
	30	2.044	0.128
	40	1.892	0.476
	60	2.020	0.401
$Z = 0.014$			
	15	1.656	0.162
	18	1.708	0.067
	25	1.719	0.337
	30	2.643	0.396
	40	2.380	0.155
	60	1.828	0.099
$Z = 0.02$			
	15	1.626	0.054
	18	1.739	0.087
	25	1.991	0.346
	30	2.129	0.166
	40	2.337	0.487
	60	2.895	0.514

2.4 Discussion and Conclusions

The two explodability criteria presented in Sect. 2.2 and 2.3 agree quite well for 21 models out of 27. The 6 models that have a different fate depending on which classification is considered are listed in Table 2.3 among the others. For the $60\,M_\odot$ model with metallicity $Z = 0.001$ the classification from Ertl et al. (2016) gives a successful explosion only for three separation lines out of five, but even for the other two the models locates very close to the separation line, therefore its outcome is uncertain. It is worth noting that this model is the only one, among those 6 with a different possible outcome, for which the compactness classification predicts a BH formation while the $M_4 - \mu_4$ classification predicts an explosion. This could be due to the fact that this model has the lowest μ_4 value among models with same metallicity, which highly favors the explosion, and this can not be taken into account in the one parameter classification which looks only for the compactness of the model. For all other five

the outcome is exactly the opposite: the first classification gives a SN explosion as outcome, while the second one gives the formation of a BH.

As showed before, the two-parameter classification captures better the explodability of a star since it reflects both aspects of having a high mass accretion rate. On one hand the neutrino luminosity is enhanced and so the neutrino streaming from the PNS has greater chance to reenergize the stalled shock and launch the explosion of the star; on the other hand there is a higher ram pressure of the infalling layers that has to be overcome.

High compactness $\xi_{2.5}$ shows a tendency to correlate with BH formation, but there is not a sharp boundary value that separates explosions from non-explosions and also the $\xi_{2.5} - M_{ZAMS}$ relation is highly non-monotonic (Ugliano et al. 2012; Ertl et al. 2016). Conversely, in the $M_4\mu_4 - \mu_4$ plane this separation does exist and it is represented by the separation line.

In Table 2.3 the M_{pre-SN} and the M_{Fe} of all the progenitors are listed. For models that form a black hole the M_{pre-SN} can be taken as a good proxy of the final mass of the remnant, since the fallback in Ertl et al. (2016) is mostly inefficient. Regarding the iron core mass, this can be a reasonable approximation to the mass of the neutron star that results from a successful SN explosion. Under these assumptions the successful SN models in my grid are expected to produce NS with masses in the range from $\sim 1.5\,M_\odot$ to $\sim 1.7\,M_\odot$. Such values overlap with the estimated interval of NS masses ($\sim 1.1 - 1.6\,M_\odot$) derived from the NS-NS merger event (GW170817, Abbott et al. 2017).

In respect to the models that go through the BH channel, it is interesting to compare our predictions with the results from other gravitational-wave emission events. In particular, BH with masses of $\sim 36\,M_\odot$ and $\sim 29\,M_\odot$, that characterize the components of the BH-BH merger (GW150914, Abbott et al. 2016) are expected to be produced by my models with $M_{ZAMS} = 30, 40\,M_\odot$ and $Z = 0.001$, $M_{ZAMS} = 30, 40\,M_\odot$ and $Z = 0.006$, $M_{ZAMS} = 40, 60\,M_\odot$ and $Z = 0.014$. Just recently, another merging event between two compact objects has been detected (GW190814, Abbott et al. 2020). The BH component with mass of $\sim 23\,M_\odot$ is consistent with a stellar progenitor of $M_{ZAMS} = 25\,M_\odot$ and $Z = 0.001$, $M_{ZAMS} = 25\,M_\odot$ and $Z = 0.006$, $M_{ZAMS} = 30\,M_\odot$ and $Z = 0.014$, $M_{ZAMS} = 40, 60\,M_\odot$ and $Z = 0.02$. As to the other mysterious compact object of mass $\sim 2.6\,M_\odot$, I notice that an iron core of similar mass is left at the end of the pre-supernova evolution of the model with $M_{ZAMS} = 60\,M_\odot$ and $Z = 0.02$.

Of course the only way to have a confirmation about the fate of these models would be to perform collapse and explosion simulations in one or more dimensions and then compare the results with those discussed here. Both classifications are based on caveats and approximations especially regarding the neutrino-driven mechanism, since the current understanding of the latter is not complete, and they are developed from a 1D modeling approach that can not take into account multi-dimensional effects. However, significant progress has been achieved in both 2D and 3D simulations which may improve our understanding of the physical processes involved in SN explosions and BHs formation. Hopefully in the future large sets of 3D explosion simulations will be feasible.

Table 2.3: values of M_{ZAMS}, M_{pre-SN} and M_{Fe} for all the models subdivided according to the initial metallicity. In the last two columns to the right there are the likely outcomes of the progenitors according to the mono-parametric and the bi-parametric criterion respectively.

	M_{ZAMS} $[M_\odot]$	M_{pre-SN} $[M_\odot]$	M_{Fe} $[M_\odot]$	$\xi_{2.5}$	$M_4\mu_4 - \mu_4$
$Z = 0.001$					
	15	14.742	1.686	NS	BH
	18	17.748	1.845	BH	BH
	25	24.526	1.874	BH	BH
	30	29.452	2.060	BH	BH
rot	30	17.773	2.432	BH	BH
	40	38.647	2.002	BH	BH
	60	54.548	2.007	BH	NS
rot	60	17.658	2.100	BH	BH
cf88	60	54.594	2.197	BH	BH
$Z = 0.006$					
	15	13.773	1.547	NS	NS
	18	16.498	1.641	NS	BH
	25	23.572	1.660	NS	BH
	30	26.409	1.887	BH	BH
	40	28.714	2.249	BH	BH
	60	46.366	2.034	BH	BH
$Z = 0.014$					
	15	13.234	1.612	NS	BH
	18	16.707	1.638	NS	NS
	25	18.992	2.173	BH	BH
	30	21.929	2.219	BH	BH
	40	26.217	2.099	BH	BH
	60	35.951	1.760	NS	BH
$Z = 0.02$					
	15	13.193	1.568	NS	NS
	18	16.482	1.646	NS	NS
	25	19.300	1.830	BH	BH
	30	17.882	1.906	BH	BH
	40	24.399	2.201	BH	BH
	60	24.612	2.634	BH	BH

Chapter 3

Stellar Evolution Models

Modules for Experiments in Stellar Astrophysics (MESA) is an open source stellar evolution package used by a large community of astrophysicists undergoing continuous and constant development (Paxton et al. 2011, 2013, 2017, 2018, 2019). MESA has a new one dimensional (1D) stellar evolution code, MESA star (Paxton et al. 2011), but is designed such that each of its single components, modules, can be used on its own, characteristic that makes it easier to test and compare between its different modules and other already existing stellar evolution codes, e.g. KEPLER (Heger et al. 2005), STERN (Petrovic et al. 2005). Each thread-safe[1] module deals with a different aspect of numerical methods or physics, while the MESA star module is the one responsible for the evolution of the model. It calls all the needed modules in order to be able to solve the highly non-linear stellar structure and composition equations at every timestep. The possible uses of MESA cover a broad range of stellar astrophysics topics that can vary from asteroseismology and variables stars to giant planets evolution, as well as helium core flash in low mass stars, binary stars, core-collapse supernovae and their light curves, black holes formation and many more.

For these work I use MESA version r12115 compiled with GNU Fortran 9.2.0 which is part of MESA SDK-20190830. In the following sections there is an overview of the relevant physics adopted in the models and their implementation in MESA including, among others, microphysics, mixing processes and mass loss.

3.1 Microphysics

3.1.1 Equation of State (ESO)

The EOS tables in MESA are based on the OPAL EOS tables (Rogers & Nayfonov 2002) with smoothly transition to the SCVH tables (Saumon et al. 1995) at lower temperatures and densities. The extended MESA EOS tables cover $X = 0.0$, 0.2, 0.4, 0.6, 0.8, and 1.0 and $Z = 0.0$, 0.02, and 0.04. The PTEH option (Pols et al. 1995) extends the eos coverage to lower densities (to $10^{-18} g \cdot cm^{-3}$) and higher metallicities (Z up to 1.0). The HELM tables (Timmes & Swesty 2000), which are used even in higher temperature regimes, and PC tables (Potekhin & Chabrier 2010) are used at higher densities with respect to OPAL+SCVH+PTEH.

[1] multiple processes can execute the module simultaneously

In my simulations I use these other two eos options: DT2 (with a linear interpolation to HELM) and ELM. The first one is a second way to access OPAL/SCVH data using density and temperature as variables, while the second is a subset of HELM. So ELM is used in high ρ and T regions where otherwise would be used HELM.

3.1.2 Opacities

MESA divides the radiative opacity tables into two temperature regimes, high ($logT \gtrsim 4$) and low ($logT \lesssim 4$), and treats them separately. This system allows the user to choose, for the low temperature opacities, between either Ferguson et al. (2005) or Freedman et al. (2008) with updates to ammonia opacity from Yurchenko et al. (2011) and the pressure induced opacity for molecular hydrogen from Frommhold et al. (2010). The high temperature opacity tables come from either OPAL (Iglesias & Rogers 1993, 1996) or OP (Seaton 2005). The OPAL tables are split into two types, Type I and Type II: Type I tables are used for $0.0 \leq X \leq 1.0 - Z$ and $0.0 \leq Z \leq 0.1$ for a fixed abundance pattern; Type II tables are optionally available which allow enhanced carbon and oxygen abundances in addition to those already accounted for in Z, covering $0.0 \leq X \leq 0.7$ and $0.0 \leq Z \leq 0.1$. Type II opacities are particularly important for helium burning and beyond. To use Type2 opacities one needs to specify a base metallicity, Zbase, which gives the metal abundances previous to any CO enhancement. The electron conduction opacity tables are originally based on Cassini et al. (2007), but they have been extended to cover temperatures up to $10^{10}\,K$ and densities up to $10^{11.5}\,g \cdot cm^{-3}$ (Paxton et al. 2013).

I use the Ferguson et al. (2005) low temperature tables (*kappa_lowT_prefix=lowT_fa05_gs98*) and the OPAL Type I tables, then gradually switch to the OPAL Type II opacities (*kappa_file_prefix=gs98*), setting in every simulation the value of Zbase equal to the Z one's.

3.1.3 Nuclear Network

From Paxton et al. (2019) the *Joint Institute for Nuclear Astrophysics* (JINA) REACLIB library has been updated from the *jina_reaclib_results_v2.2* snapshot to the *jina_reaclib_results_20171020_defalut* snapshot. So the default choice for the rate in MESA is the so called NACRE library from Angulo et al. (1999) for $T < 10^7\,K$ and the above mentioned *jina_reaclib_results_20171020_defalut* for $T > 1.1 \cdot 10^7\,K$, while in the region between the two temperatures is used a blend over the two rates. For example the default rate of $^{12}\mathrm{C}(\alpha,\gamma)^{16}\mathrm{O}$ at $T = 10^9\,K$, i.e. from jina reaclib, is $6.454310 \cdot 10^{-6}\,cm^3/mol \cdot s$.

Only in one model I set the rate of the latter reaction to a different value in order to study the changes that this choice implies. The new rate is from CF88 library from Frank Timmes's version of Caughlin & Fowler(1988) and its value, as above at $T = 10^9\,K$, is $3.7150542 \cdot 10^{-6}\,cm^3/mol \cdot s$. I use the *basic.net* nuclear network in MESA for hydrogen and helium network, which includes 8 isotopes: ^{1}H, ^{3}He, ^{4}He, ^{12}C, ^{14}N, ^{16}O, ^{20}Ne and ^{24}Mg. Then MESA automatically extends the network. For carbon-oxygen network it is employed the *co_burn.net* file which is formed by *basic.net* plus the ^{28}Si isotope; afterwards for the advanced network it is used *approx21.net* composed of *co_burn.net* plus ^{36}Ar, ^{40}Ca, ^{44}Ti, ^{48}Cr, ^{52}Fe, ^{54}Fe, ^{56}Ni, ^{56}Fe and ^{56}Cr isotopes. Finally, roughly at the half of the

silicon burning phase, I change for the last time the nuclear network to *approx21_cr60_plus_co56* which intuitively simply adds two more isotopes: ^{56}Co and ^{60}Cr.

3.2 Boundary Conditions

The pressure and temperature in the outermost cell of stellar model calculation must be specified as a set of boundary conditions, this is done through the atm module in MESA. The command *atm_options* controls how the surface temperature T_{surf} and pressure P_{surf} are evaluated when setting up outer boundary conditions. I select the *T_tau* option: the atmosphere structure is solved with a given $T(\tau)$ relation which in this case is the grey Eddington relation:

$$T^4(\tau) = \frac{3}{4}T_{eff}^4\big(\tau + \frac{2}{3}\big), \tag{3.1}$$

where T_{eff} is calculated directly from the MESA interior model. Similarly, P is computed as follows:

$$P = \frac{\tau g}{\kappa}\big[1 + P_0\frac{\kappa}{\tau}\frac{L}{M}\frac{1}{6\pi cG}\big]. \tag{3.2}$$

The second term in the square brackets accounts for the nonzero radiation pressure (e.g. Cox 1968) which can be significant in high mass stars. P_0 is a dimensionless factor of order unity used to scale up the radiation pressure in order to help convergence in massive stars radiating close to or at super-Eddingthon luminosity. Inside MESA P_0 is called *Pextra_factor* which if set to a negative number means that would be used the (incorrect) old form $1.6{\cdot}10^{-4}\kappa\big(\frac{L/L_\odot}{M/M_\odot}\big)$ for the nonzero radiation pressure. I adopt $P_0 = -1$ in this work and an opacity fixed to the one of the outermost cell of the interior model.

3.3 Diffusion

For a plasma species (i.e., electrons and ions) the unmodified Burgers (1969) equations for diffusion are solved in cgs units. The form of the diffusion solver closely follows the general approach presented by Thoul et al. (1994) for arranging the full set of equations into a single matrix equation but it enters the Burgers equations into that matrix structure without rescaling any quantities, therefore any additional ideal-gas assumptions beyond those already present in the Burgers equations is avoided. By default MESA uses the Paquette et al. (1986a) coefficients for electron-ion terms and adopts Stanton & Murillo (2016) for all ion-ion coefficients. Also by default the diffusion is shut off for $\Gamma \geq 175$, with Γ the Coulomb coupling parameter, and gradually decreased as gamma increases from 150 to 175 so there is no diffusion when the ions are well into liquid regime.

3.4 Rotation

Rotation affects the evolution of a star since it modifies the star's thermal equilibrium (von Zeipel 1924) and induces dynamical and secular instabilities (Maeder & Meynet 2000b). Those effects are enhanced by the increasing of radiation pressure which makes rotation even more important in massive stars such as those investigated in this work (Heger et al. 2000). Rotation plays a determinant role, according to its importance, in the final fate of the star (Heger et al. 2005; Woosley & Heger 2006).

In MESA rotation is implemented through the so called shellular approximation (Meynet & Maeder 1997), which states that the angular velocity of the star is constant over isobars. Using this approximation it is allowed to solve the stellar structure in one dimension even though the structure of the rotation is of course three dimensional. Resulting from that the stellar equations are modified with the add of centrifugal acceleration terms when rotation is present.

The only two rotating models, $30\,M_{\odot}$ star and $60\,M_{\odot}$ star with metallicity $Z = 0.001$, are both initialized with solid body rotation on the zero age main sequence (the standard choice, see e.g. Heger et al. 2000) through the parameter $\Omega/\Omega_c = 0.7$, where Ω the surface angular velocity and Ω_c the surface critical angular velocity defined as:

$$\Omega_c^2 = \Gamma_{Edd}\frac{GM}{R^3}, \tag{3.3}$$

with the Eddington gamma-factor defined as $\Gamma_{Edd} = 1 - min(L/L_{Edd}, 0.9999)$ where L_{Edd} is the Eddington luminosity of the star.

In Sect. 3.5.4 are discussed chemical mixing and angular momentum transport due to rotation, while in Sect. 1.2.3 is discussed the enhancement of the mass loss due to rotation.

3.5 Mixing Processes

3.5.1 Convection

Mixing Lenght Theory (MLT) describes the convective transport of energy in the stellar interior. There is a crucial free parameter of order unity , α_{MLT}, that determines how far a fluid parcel travels before dissolving into backgrounds. It parametrizes how efficient convection is. I set this parameter to 1.5 and from when $log(\rho_c) > 9.90$ onward to 1.89.

Convective mixing is treated as a time-dependent diffusive process with a diffusion coefficient computed within the MLT formalism. I adopt the modified version of MLT from Henyey et al. (1965) instead of standard MLT prescription (Cox 1968), as the latter assumes no radiative losses from fluid elements and is therefore applicable only at high optical depth. Besides α_{MLT} there are two free parameters, ν and y, which are multiplicative factors to the mixing lenght velocity and temperature gradient in the convective element. They are set respectively to 8 and 1/3 (Henyey et al. 1965). This framework allows convective efficiency to vary with the opacity of the convective element.

Usually, the location of the convective region is determined using the Schwarzschild criterion, which implies that a region is convectively stable if

$$\nabla_T < \nabla_{ad}, \tag{3.4}$$

where ∇_T is the local background temperature gradient and ∇_{ad} is the adiabatic temperature gradient. Alternatively, the Schwarzschild criterion can be replaced by the Ledoux criterion, which also takes into account the composition gradient, ∇_μ. In this case, a region is convectively stable if

$$\nabla_T < \nabla_L \tag{3.5}$$

$$\nabla_L = \nabla_{ad} - \frac{\chi_\mu}{\chi_T}\nabla_\mu \tag{3.6}$$

$$\chi_\mu = \Big[\frac{\partial ln(P)}{\partial ln(\mu)}\Big]_{\rho,T} \tag{3.7}$$

$$\chi_T = \Big[\frac{\partial ln(P)}{\partial ln(T)}\Big]_{\rho,\mu}. \tag{3.8}$$

I adopt the Ledoux criterion for convection in my models to account for the composition effects.

Until the star reaches the value of $log(\rho_c) = 9.90$ I use an improved version of the MLT, namely the MLT++ treatment of convection (Paxton et al. 2013), in order to take into account the fact that the superadiabatic gradient in radiation-dominated envelopes can force the adoption of prohibitively short timesteps. This new implementation allows to reduce the superadiabaticity in some radiation-dominated convective regions and hence it makes easier to calculate models of massive stars.

3.5.2 Overshoot Mixing

To model the mixing occurring at convective boundaries, also known as overshoot mixing, one must turn to yet another set of parameterizations. Typically, a convective region is extended beyond the fiducial boundary determined by either the Schwartzschild or Ledoux criterion in order to account for the nonzero momentum of the fluid element approaching the edge of the convective zone as well as its subsequent penetration into the non-convective region. This overshoot action leads to enhanced mixing.

Following the parameterization discussed in Herwig (2000), the resulting diffusion coefficient in the overshoot region is given by

$$D_{ov} = D_0\, e^{-\frac{2z}{f_{ov} H_P}}, \tag{3.9}$$

where f_{ov} is a free parameter that determines the efficiency of overshooting mixing, H_P is the local pressure scale height, D_0 is the diffusion coefficient in the unstable region "near" the convective boundary and z is the distance in the radiative layer away from that location. A second parameter specifies better how much "near" the overshooting actually begins: it does at a distance $f_{0,ov} H_P$ into the convective zone rather than exactly at the edge. I adopt only a single set of $(f_{ov}\,, f_{0,ov})$ values for both the core and the shell/envelope of the star model, irrespective of the type of burning taking place in the overshoot region. The values used are, respectively, 0.010 and 0.004.

3.5.3 Semiconvection and Thermohaline Mixing

As stated in Section 3.5.1 I adopt the Ledoux criterion for convection in my models. Due to the additional composition gradient term, a region that is formally convectively unstable to Schwartzschild criterion may be stable according to the Ledoux criterion, which leads to a type of mixing called semiconvection. On the other hand, a thermally stable medium may have a negative, destabilizing composition gradient, which triggers an instability called thermohaline mixing. This needed inverted chemical composition gradient is however rare in stars.

In MESA, semiconvection and thermohaline mixing are both implemented as time-dependent diffusive processes. The diffusion coefficient for the semiconvection is calculated following Langer et al. (1983) (but setting the temperature gradient ∇_T equal to the radiative gradient ∇_r):

$$D_{sc} = \alpha_{sc}\Big(\frac{K}{6C_P\rho}\Big)\frac{\nabla_T - \nabla_{ad}}{\nabla_L - \nabla_T}, \tag{3.10}$$

where K is the radiative conductivity, C_P the specific heat at constant pressure and α_{sc} a dimensionless efficiency parameter. In a similar way, the diffusion coefficient for the thermohaline mixing is computed following Kippenhahn et al. (1980):

$$D_{th} = \alpha_{th}\Big(\frac{3K}{2C_P\rho}\Big)\frac{-\frac{\chi_\mu}{\chi_T}\nabla_\mu}{\nabla_T - \nabla_{ad}}, \tag{3.11}$$

where α_{th} is also a dimensionless efficiency parameter that describes the aspect ratio of the mixing blobs (a large α_{th} corresponds to slender blobs).

I adopt $\alpha_{sc} = 0.01$ and $\alpha_{th} = 2$, although for each of these two parameters there is a wide range of values accepted in literature.

3.5.4 Rotationally Induced Instabilities

In MESA transport chemicals and angular momentum due to rotation are treated in a diffusion approximation. (Heger et al. 2000; Yoon & Langer 2005). In my models there are five rotationally induced instabilities: Solberg-Høiland (SH) instability, secular shear instability, Eddington-Sweet (ES) circulation, Goldreich-Schubert-Fricke (GSF) instability and Spruit-Tayler dynamo (see Heger et al. 2000 and Paxton et al. 2013 for details). The diffusion coefficients of these processes, once calculated, are combined with those of the other mixing processes such as convection, semiconvection and thermohaline and then are used in the angular momentum and abundance diffusion equations. In this implementation there are two free parameters (Pinsonneault et al. 1989): f_c, from 0 to 1, is the ration between the diffusion coefficient and the turbulent viscosity, it scales the composition mixing to the angular momentum transport; and f_μ, which represents the sensitivity of rotational mixing to the mean molecular weight gradient ∇_μ. With a small f_c the angular momentum is transported more accurately than the material are mixed and a small f_μ means that although there is the stabilizing effect of ∇_μ the rotational mixing is still efficient. I adopt the standard values for these two parameters: $f_c = 1/30$ and $f_\mu = 0.05$ following Heger et al. (2000).

Bibliography

[1] B., Paxton & L., Bildsten (2011), *Modules for experiments in stellar astrophysics (MESA)*

[2] B., Paxton et al. (2013), *Modules for experiments in stellar astrophysics (MESA): planets, oscillations, rotation, and massive stars*

[3] B., Paxton et al. (2017), *Modules for experiments in stellar astrophysics (MESA): binaries, pulsations, and explosions*

[4] B., Paxton et al. (2018), *Modules for experiments in stellar astrophysics (MESA): convective boundaries, element diffusion, and massive stars explosions*

[5] B., Paxton et al. (2019), *Modules for experiments in stellar astrophysics (MESA): pulsating variable stars, rotation, convective boundaries, and energy conservation*

[6] Frank Timmes's version of G. R., Caughlin & W. A., Fowler (1988), *Atom. Data and Nuc. Data Tables, 40, 283*

[7] C., Angulo et al. (1999), *NACRE: A European Compilation of Reaction rates for Astrophysics*

[8] E., O'Connor & C. D., Ott (2011), *Black hole formation in failing core-collapse supernovae*

[9] T., Ertl et al. (2016), *A two-parameter criterion for classifying the explodability of massive stars by the neutrino-driven mechanism*

[10] M., Ugliano et al. (2012), *Progenitor-explosion connection and remnant birth masses for neutrino-driven supernovae of iron-core progenitors*

[11] T., Sukhbold & S. E., Woosley (2014). *The compactness of presupernova stellar cores*

[12] J., Choi et al. (2016), *Mesa isochrones and stellar tracks (mist). I: solar-scaled models*

[13] P., Girichidis et al. (2020), *Physical processes in star formation*

[14] S. E., Woosley et al. (2002), *The evolution and explosion of massive stars*

[15] M. W., Topping et al. (2020), *The MOSDEF-LRIS survey: the interplay between massive stars and ionized gas in high-redshift star-forming galaxies*

[16] R., Valiante et al. (2017), *Chasing the observational signatures of seed black holes at $z > 7$: candidates statistics*

[17] R., Valiante et al. (2018), *Chasing the observational signatures of seed black holes at $z > 7$: candidates statistics*

[18] R., Valiante et al. (2018), *Chasing the observational signatures of seed black holes at $z > 7$: candidates observability*

[19] K., Nomoto (2012), *Final fates of massive stars*

[20] L. B., Lucy & P. M., Solomon (1967), *Mass loss from O and B supergiants*

[21] J. I., Castor et al. (1975), *Radiation-driven winds in O stars*

[22] D. C., Abbott (1982), *The theory of radiation driven stellar winds and the Wolf-Rayet phenomenon*

[23] D. B., Friend & D. C., Abbott (1986), *The theory of radiation driven stellar winds. III. Wind models with finite disk correction and rotation*

[24] A., Pauldrach et al. (1986), *Radiation-driven winds of hot luminous stars. Improvements of the theory and first results*

[25] R. P., Kudritzki et al. (1989), *Radiation-driven winds of hot stars. VI. Analytical solutions for wind models including the finite cone angle effect*

[26] H. J. G. L. M., Lamers (2007), *The theory of line driven stellar winds*

[27] H. J. G. L. M., Lamers & J. P., Cassinelli (1997), *Introduction to stellar winds*

[28] C. J. E., Wolf & G., Rayet (1867), *Spectroscopie stellaire*

[29] C., Georgy et al. (2015), *Wolf-Rayet stars as an evolved stage of stellar life*

[30] G., Meynet & A., Maeder (2003), *Stellar evolution with rotation X. Wolf-Rayet star populations at solar metallicity*

[31] E., Glebbeek et al. (2009), *The evolution of runaway stellar collision products*

[32] J. S., Vink et al. (2000), *New theoretical mass-loss rates of O and B stars*

[33] J. S., Vink et al. (2001), *Mass-loss predictions for O and B stars as a function of metallicity*

[34] T., Nugis & H. J. G. L. M., Lamers (2000), *Mass-loss of Wolf-Rayet stars as a function of stellar parameters*

[35] C., de Jager et al. (1988), *Mass loss rates in the Hertzsprung-Russell diagram*

[36] N., Mauron & E., Josselin (2011), *The mass-loss rates of red supergiants and the de Jager prescription*

[37] A., Heger et al. (2000), *Presupernova evolution of rotating massive stars. I. Numerical method and evolution of the internal stellar structure*

[38] M., Limongi (2017), *Supernovae from massive stars*

[39] S. E., Woosley et al. (2007), *Pulsation pair instability as an explanation for the most luminous supernovae*

[40] H. T., Janka (2017), *Neutrino-driven explosions*

[41] S. E., Woosley et al. (1988), *Supernova 1987A: six weeks later*

[42] S. E., Woosley et al. (1997), *SN 1987A - Presupernova evolution and the progenitor star*

[43] T., Shigeyama & K., Nomoto (1990), *Theoretical light curve of SN 1987A and mixing of hydrogen and nickel in the ejecta*

[44] A., Heger et al. (2005), *Presupernova evolution of differentially rotating massive stars including magnetic field*

[45] J., Petrovic et al. (2005), *Which massive stars are gamma-ray burst progenitors?*

[46] F. J., Rogers & A. Nayfonov (2002), *Updated and expanded OPAL equation-of-state tables: implications for helioseismology*

[47] D., Saumon et al. (1995), *An equation of state for low-mass stars and giant planets*

[48] O. R., Pols et al. (1995), *Approximate input physics for stellar modelling*

[49] F. X., Timmes & F. D., Swesty (2000), *The accuracy, consistency, and speed of an electron-positron equation of state based on table interpolation of the Helmholtz free energy*

[50] A. Y., Potekhin & G., Chabrier (2010), *Thermodynamic functions of dense plasma: analytic approximations for astrophysical applications*

[51] J. W., Ferguson et al. (2005), *Low-temperature opacities*

[52] R. S., Freedman et al. (2008), *Line and mean opacities for ultracool dwarfs and extrasolar planets*

[53] S. N., Yurchenko et al. (2011), *A variationlly computed line list for NH_3*

[54] L., Frommhold et al. (2010), *Infrared atmospheric emission and absoprtion by simple molecular complexes, from first principles*

[55] C. A., Iglesias & F. J., Rogers (1993), *Radiative opacities for carbon- and oxygen-rich mixtures*

[56] C. A., Iglesias & F. J., Rogers (1996), *Updated Opal opacities*

[57] M. J., Seaton (2005), *Opacity project data on CD for mean opacities and radiative accelerations*

[58] S., Cassini et al. (2007), *Updated electron-conduction opacities: the impact on low-mass stellar models*

[59] Cox, J. P. (1968), *Principles of stellar structure - Vol.1: Physical principles; Vol.2: Applications to stars*

[60] J. M., Burgers (1969), *Flow equations for composite gases*

[61] A. A., Thoul et al. (1994), *Element diffusion in the solar interior*

[62] C., Paquette et al. (1986), *Diffusion coefficients for stellar plasmas*

[63] L. G., Stanton & M. S., Murillo (2016), *Ionic transport in high-energy-density matter*

[64] H., von Zeipel (1924), *The radiative equilibrium of slightly oblate rotating star*

[65] A., Maeder & G., Meynet (2000), *The evolution of rotating stars*

[66] S. E., Woosley & A., Heger (2006), *The progenitor stars of gamma-ray bursts*

[67] G., Meynet & A., Maeder (1997), *Stellar evolution with rotation. I. The computational method and the inhibiting effect of the μ-gradient*

[68] L., Henyey et al. (1965), *Studies in stellar evolution. III. The calculation of models envelopes*

[69] F., Herwig (2000), *The evolution of AGB stars with convective overshoot*

[70] N., Langer et al. (1983), *Semiconvective diffusion and energy transport*

[71] R., Kippenhahn et al. (1980), *The time scale of thermohaline mixing in stars*

[72] S. -C., Yoon & N., Langer (2005), *Evolution of rapidly rotating metal-poor massive stars towards gamma-ray bursts*

[73] M. H., Pinsonneault et al. (1989), *Evolutionary models of the rotating Sun*

[74] S. E., Woosley & T. A., Weaver (1995), *The evolution and explosion of massive stars II: explosive hydrodynamics and nucleosynthesis*

[75] M., Limongi & A., Chieffi (2006), *The nucleosynthesis of ^{26}Al and ^{60}Fe in solar metallicity stars extending in mass from 11 to 120 $M_{\odot}$: the hydrostatic and explosive contributions*

[76] K., Nomoto et al. (2006), *Nucleosynthesis yields of core-collapse supernovae and hypernovae, and galactic chemical evolution*

[77] B. P., Abbott et al. (2016), *GW150914: first results from the search for binary black holes coalescence with advanced LIGO*

[78] B. P., Abbott et al. (2016), *GW151226: observation of gravitational waves from a 22-solar-mass binary black hole coalescence*

[79] B. P., Abbott et al. (2017), *GW170817: observation of gravitational waves from a binary neutron stars inspiral*

[80] R., Abbott et al. (2020), *GW190814: gravitational waves from the coalescence of a 23 solar mass black hole with a 2.6 solar mass compact object*